Eddy Train Encounters with a Continental Boundary: A South Atlantic Case Study

3/23/12

José L. L. Azevedo[1], Doron Nof[2,3*] and Mauricio M. Mata[1]

[1] Laboratório de Estudos dos Oceanos e Clima, Instituto de Oceanografia, Universidade Federal do Rio Grande-FURG, Rio Grande (RS), Brazil.

[2] Department of Earth, Ocean and Atmospheric Science, Florida State University, Tallahassee (FL), United States.

[3] Geophysical Fluid Dynamics Institute, Florida State University, Tallahassee (FL), United States.

*Corresponding author email: nof@ocean.fsu.edu

ABSTRACT

Satellite altimetry suggests that large anticyclonic eddies (rings) originating from the Agulhas Current retroflection occasionally make their way across the entire South Atlantic Ocean. What happens when these rings encounter a western boundary current? In this work, interactions between a "train" of nonlinear lens-like eddies and a Southern Hemisphere continental boundary are investigated analytically and numerically on a β plane. The train of eddies is modeled as a steady double-frontal zonal current with the same vorticity and transport as the eddies themselves. The continental boundary is represented by a vertical wall, which is purely meridional in one case and is tilted with respect to the north in another case. It is demonstrated analytically that the eddy–wall encounter produces an equatorward flow parallel to the continental wall, thus suggesting a weakening of the transport of the associated (poleward-flowing) western boundary current upstream of the encounter zone and unchanged transport downstream. A large stationary eddy is established in the contact zone because its β-induced force is necessary to balance the other forces along the wall. The size of this eddy is directly proportional to the transport of the eddy train and the meridional tilt of the wall. These scenarios are in good agreement with results obtained numerically using an isopycnal Bleck and Boudra model.

1. Introduction

Migration of eddies in the ocean can be induced by several mechanisms. The primary mechanism results from latitudinal variation of the Coriolis parameter, which imposes a westward drift on oceanic eddies (e.g., Flierl 1979; Nof 1981; Killworth 1983; Cushman-Roisin et al. 1990). Advection by surrounding currents and propulsion related to neighboring eddies or sea bottom topography (i.e., topographic β) can also induce eddy movement. Chelton et al. (2007, 2011) clearly documented westward eddy drift across the world's oceans, showing large eddies moving westward via nearly zonal propagation routes. Chelton et al. (2011) found that 75% of 36,000 eddies analyzed worldwide propagated toward the west, implying inevitable encounters of some of these eddies with continental boundaries (see their Figs. 4d–4f).

a. Observational background

The eddy-tracking dataset of Chelton et al. (2011; available at http://cioss.coas.oregonstate.edu/eddies/) allows us to follow eddy trajectories through 16 years of sea level anomaly fields (14 October 1992 to 31 December 2008). Fig. 1A shows the trajectories of ten eddies that originated in the Agulhas retroflection zone and crossed the South Atlantic Ocean during this time. Eddy collisions with the South American continental boundary seem inevitable, which raises a number of questions: If such collisions do occur, what processes are involved? What are the governing forces, and how do these encounters influence the western ocean boundary? Do eddy interactions, for example, potentially influence the variability of the Brazil Current (BC)?

The Agulhas Current sheds four to six eddies per year to the South Atlantic Ocean (e.g., Beal et al. 2011), where some have been observed to have a residence time of three to four years (Byrne et al. 1995). Such eddies have typical radii of 70–170 km and depths of 500–1000 m [determined using data from Duncombe Rae (1991), Goni et al. (1997), McDonagh et al. (1999), Garzoli et al. (1999), Pichevin et al. (1999), Lutjeharms (2006), and Chelton et al. (2011)]. As is typical for eddies formed by a retroflection, Agulhas eddies are larger than most other eddies in the world ocean (e.g., Nof and Pichevin 1996). Like Gulf Stream eddies, they are commonly referred to as “rings.” The water carried by these eddies into the South Atlantic Ocean defines the Agulhas leakage, which plays a crucial role in global ocean circulation and climate (e.g., Biastoch et al. 2009; Beal et al. 2011). Despite the importance of this leakage, estimates of its magnitude are highly uncertain, ranging between 2 and 15 Sv (e.g., Beal et al. 2011).

The ring-shedding process begins with the injection of low-density surface water from the Agulhas retroflection into the Cape Basin. As the retroflection meander further develops, the resulting flow breaks up, thus producing isolated rings. The waters within the ring, anomalous in nature relative to the surrounding ocean waters, are confined from below by a concave-up density interface that intersects the ocean surface along a closed contour. This confinement forms an isolated, low-density feature referred to here as a “lens.” This lens is characterized by an interior anticyclonic circulation and zero thickness at the rim and everywhere beyond. Due to the rings' large initial volumes, it is expected that they would possess a mass sufficient to affect BC transport upon their arrival at the South American continental boundary (Fig. 1B) despite ring decay during the ocean crossing. This scenario, with a “train” of lens-like eddies making contact with the continental boundary, is the focus of this work.

b. Southwestern Atlantic

Encounters between Agulhas rings and the South American continental boundary, including the Brazil Current (Fig. 2), are an important part of the intriguing South Atlantic circulation puzzle. These complex interactions may influence the observed latitudinal drift of the Brazil–Malvinas Confluence Zone (BMCZ) and the formation of intrusion eddies. Various studies suggest that drift of the BMCZ is due to variations in the relative transports of the converging Brazil and Malvinas currents (Agra and Nof 1993; Matano 1993; Lebedev and Nof 1996; Lebedev and Nof 1997; Witter and Gordon 1999; Wainer et al. 2000; Lentini et al. 2002). Arruda et al. (2002) suggest that temporal variations in BC transport upstream of the zone can affect the detachment of intrusion eddies at the BMCZ. The shedding of Agulhas rings and their eventual coalescence with the BC may, through a transoceanic "domino effect,", contribute to the observed variability. This linked sequence of events, analogous to a falling row of dominoes, could serve to connect the Agulhas and southwestern Atlantic regions: (1) shedding of rings at the Agulhas Retroflection zone, (2) transatlantic crossing and coalescence of some of those rings with the BC, (3) modulation of BC transport, (4) modification of the balance (relative transports) of the BC and MC at the confluence zone, (5) latitudinal drift of the BMCZ, and (6) variation in the frequency of intrusion-ring shedding.

Despite recent progress in the observation and modeling of western boundary current processes, the fate of Agulhas rings that cross the South Atlantic and collide with the South American continental boundary remains poorly described and understood. In this work, we employ analytical and numerical modeling to explore some aspects of these collisions. The eddies are modeled as lenses forming an "eddy train"—a sequence of identical, uniformly spaced lenses that propagate zonally toward the western boundary. Rather than model individual eddies, we introduce a novel approach involving a "double-frontal current" (DFC) with a westward flow in its northern limb and an opposite flow in its southern limb, resulting in a current with the same vorticity and net transport as the eddy train.

This paper is organized as follows: In section 2, a review of eddy–wall interactions is presented. Section 3 briefly develops the governing equations used in this study. Sections 4 and 5 investigate analytically and then numerically the eddy–wall encounter. Finally, in section 6, the study results are discussed and conclusions are presented.

2. Modeling Background

The eddy–wall problem has been studied by several authors (e.g., Lamb 1932; Saffman 1979; Minato 1982, 1983; Umatani and Yamagata 1987; Masuda 1988), who worked primarily with linear quasigeostrophic eddies (i.e., small-amplitude non-lenses) and encounters on an f plane. Shi and Nof (1994) summarized previous studies of an isolated eddy´s migration along a free-slip meridional wall. Also among the pioneering works, Yasuda et al. (1986) considered interactions on a β plane, mentioning the action of the β force.

Nof (1988a) proposed an analytical modeling approach for studying eddy–wall interactions, considering a barotropic eddy with a small Rossby number ($R_o << 1$) and interactions on an f plane. He concluded that after the contact, a Northern Hemisphere anticyclonic (cyclonic) eddy leaks interior fluid from its right (left) side, looking offshore. Nof (1988b) extended the investigation to interactions involving baroclinic eddies. Two types of eddies were examined: quasigeostrophic linear eddies and moderately nonlinear eddies. The former showed the same behavior as the barotropic eddies of Nof (1988a). The nonlinear eddies, however, exhibited no leak along the wall. This unexpected behavior was attributed to the high inertia of the fluid particles inside the eddy.

Shi and Nof (1993, 1994) investigated "soft" and "hard" eddy–continent interactions. Interactions due to β are relatively "soft" because the translational velocity induced in an eddy due to variation of the Coriolis parameter is notably small [~ $O(\beta R_{de}^2)$ where R_{de} is the eddy Rossby radius]. The contact of a single eddy with a continental wall is expected to last for a few weeks [~ $O(\beta R_{de})^{-1}$], the time it takes the eddy to traverse a distance equal to its own diameter. Processes not resulting from β (e.g., influences from an advective current or another vortex) can result in higher eddy velocities and stronger eddy–continent interactions. In these hard-interaction cases, eddy structure can be dramatically altered within just a few days (Shi and Nof, 1993).

Shi and Nof (1993) also examined the f-plane case. This eddy–wall interaction results in a massive leak from the eddy interior and, as expected, division of the eddy into two. The collision of an anticyclonic (cyclonic) eddy with a wall produces an offspring cyclonic (anticyclonic) eddy, with the anticyclonic (cyclonic) feature being on the left (right) side of the contact zone, looking offshore. The eddies move away from each other due to the "image effect"—i.e., each eddy is advected along the free-slip wall due to its own image (e.g., Shi and Nof 1994).

A second study (Shi and Nof 1994) investigated soft eddy–wall interactions on a β plane. Three factors were found to influence migration of the eddy along the wall (Fig. 3): the image effect, the β-induced force, and the "rocket" force. Kundu and Cohen (2008) provide a detailed discussion of the image effect. The β-induced force is due to differences in the Coriolis force acting on water particles in different eddy hemispheres. This force is always greater on the eddy's higher-latitude side, thereby resulting in a net equatorward (poleward) force in anticyclonic (cyclonic) eddies. The rocket force results when an eddy leaks its interior fluid along the wall through a thin jet. This effect is similar to that impinged on a rocket as its fuel is burnt, thereby imposing advection to the eddy in the direction opposite the leak.

Shi and Nof (1994) also considered interactions between non-lens-like quasigeostrophic eddies and a wall on an f plane. After contact, the eddy assumes the shape of a semicircle, which these researchers named a "wodon." This feature's structure is completely different from that of the eddy in the open ocean. The wodons do not leak, which led the authors to conclude that for eddies with low Rossby number (R_o), the leak does not play an important role in the interaction with the wall. The importance of the leak increases proportionally with the nonlinearity of the eddy itself.

Nof's (1999) analytical study investigated an encounter between an anticyclonic lens and a wall on a β plane. This work reported the first analytical solution that involved the image effect, the β-induced force, and the rocket force simultaneously. Surprisingly, despite previous indications that the eddy would move poleward after collision with the wall, it instead remained at a fixed latitude and slowly lost mass, leaking fluid toward the equator as it moved continually but ever more slowly toward the wall. Here, we take Nof's work a step further and tackle the eddy–wall interaction problem by using an "eddy train," a sequence of identical eddies that are evenly spaced in time.

3. Governing Equations

The momentum and mass flux balance equations for our domain (Fig. 4) are written in a convenient x–y system with the y-axis aligned with the wall. The meridional axis of the XY coordinate system is aligned with geographic north. All variables are defined here and in the appendix.

a. The momentum equation

The steady shallow-water nonlinear momentum and continuity equations of an inviscid fluid of density ρ and thickness $h(x,y)$ overlying a motionless, semi-infinite fluid of density $\rho+\Delta\rho$, where $\Delta\rho/\rho<<1$, are

Zonal Momentum
$$u\frac{\partial u}{\partial x}+v\frac{\partial u}{\partial y}-fv=-g'\frac{\partial h}{\partial x} \tag{1}$$

Meridional Momentum
$$u\frac{\partial v}{\partial x}+v\frac{\partial v}{\partial y}+fu=-g'\frac{\partial h}{\partial y} \tag{2}$$

Continuity
$$\frac{\partial(hu)}{\partial x}+\frac{\partial(hv)}{\partial y}=0\ , \tag{3}$$

where g', the reduced gravity, is defined by $g' = (g\Delta\rho)/\rho$; u and v are the zonal and meridional velocities; and f is the Coriolis parameter.

When Eqs. (1) and (2) are multiplied by height and integrated over the whole domain D_o (with area S), they become

$$\iint_S \frac{\partial(hu^2)}{\partial x}dxdy+\iint_S \frac{\partial(huv)}{\partial y}dxdy-\iint_S f_0\frac{\partial\psi}{\partial x}dxdy$$
$$-\iint_S \frac{\partial(\beta Y\psi)}{\partial x}dxdy+\iint_S \psi\beta\frac{\partial Y}{\partial x}dxdy=-\frac{g'}{2}\iint_S \frac{\partial(h^2)}{\partial x}dx\,dy$$

(4)

$$\iint_S \frac{\partial(huv)}{\partial x}dxdy+\iint_S \frac{\partial(hv^2)}{\partial y}dxdy-\iint_S f_0\frac{\partial\psi}{\partial y}dxdy$$
$$-\iint_S \frac{\partial(\beta Y\psi)}{\partial y}dxdy+\iint_S \psi\beta\frac{\partial Y}{\partial y}dxdy=-\frac{g'}{2}\iint_S \frac{\partial(h^2)}{\partial y}dxdy \tag{5}$$

where ψ is a streamfunction defined by $\partial\psi/\partial x = vh$ and $\partial\psi/\partial y = -uh$. In Eqs. (4) and (5), the Coriolis parameter is given by $f = f_0+\beta(Y-Y_0)$ where f_0 is the value at the central latitude Y_0 of the domain and β is a latitudinal correction. With the aid of Stokes Theorem and considering $Y(x,y) = -x\sin\theta + y\cos\theta$, these zonal and meridional equations become, respectively,

$$\oint_{\phi} huv\,dx - \oint_{\phi}[hu^2 + g'h^2/2 - (f_0 + \beta Y)\psi)]dy + \beta\sin\theta\iint_S \psi\,dx\,dy = 0$$

(6)

$$\oint_{\phi} huv\,dy - \oint_{\phi}[hv^2 + g'h^2/2 - (f_0 + \beta Y)\psi)]dx + \beta\cos\theta\iint_S \psi\,dx\,dy = 0\,.$$

(7)

Here, the symbol ϕ indicates the boundary of the domain (Fig. 4), and the arrowed circles represent counterclockwise integration. Specifying the boundaries, these equations can be written as

$$\begin{aligned}&\int_B^C [hu^2 + g'h^2/2 - (f_0 + \beta Y)\psi]dy + \int_D^A [hu^2 + g'h^2/2 - (f_0 + \beta Y)\psi]dy \\ &-\beta\sin\theta\iint_S \psi\,dx\,dy = 0\end{aligned} \tag{8}$$

$$\begin{aligned}&\int_B^C huv\,dy - \int_A^B \left[hv^2 + g'h^2/2 - (f_0 + \beta Y)\psi\right]dx \\ &-\int_C^D \left[hv^2 + g'h^2/2 - (f_0 + \beta Y)\psi\right]dx + \beta\cos\theta\iint_S \psi\,dx\,dy = 0\ .\end{aligned} \tag{9}$$

Eq. (8), which results from integration of the zonal momentum equation (Eq. 1), does not yield useful information because it involves an unknown force exerted on the wall (the second term). We therefore focus our attention on Eq. (9). The first term in the equation can be expressed in the *XY* system, which is indicated by the asterisks:

$$\begin{aligned}&\sin\theta\int_{Y_B}^{Y_C} h^*(u^*)^2 dY - \int_A^B \left[hv^2 + g'h^2/2 - (f_0 + \beta Y)\psi\right]dx - \\ &-\int_C^D \left[hv^2 + g'h^2/2 - (f_0 + \beta Y)\psi\right]dx + \beta\cos\theta\iint_S \psi\,dx\,dy = 0\ .\end{aligned} \tag{10}$$

Eq. (10) allows us to analyze the problem without solving the complex nonlinear equations inside the domain. Fig. 5 (left panel) shows the forces acting on the domain during impingement of the westward current on the wall. Each wall-parallel force component (black arrows) is associated with a corresponding term in Eq. (10). The first term gives the wall-parallel component of the original zonal force exerted on D_o by the westward current (WC). When θ = 0º, the value of this term is zero. The second and third terms describe the SC and NC forces exerted on D_o by currents entering or exiting through the southern and northern boundaries, respectively. These two forces operate along the axis of current flow. The fourth term, the wall-parallel component of the β force, is due to an as yet unknown permanent eddy inside the domain and will be discussed further below.

b. The mass equation

Integration of the steady continuity equation for shallow water over the whole domain D_o is

$$\int_{Y_B}^{Y_C} h^* u^* \, dY - \int_A^B hv \, dx - \int_C^D hv \, dx = 0 \,. \tag{11}$$

The first term represents transport into the domain through its eastern boundary. The next two terms represent transports across the southern (AB) and northern (CD) boundaries. Fig. 5 (right panel) shows the transports T_{BC}, T_{AB}, and T_{CD} associated with these terms.

4. The Eddy–Wall Encounter

We now consider two scenarios, one with a meridional wall (θ = 0º) and one with a wall tilted with respect to the north (θ > 0º). The latter case is more generally representative of the South American continental boundary (Fig. 2). The trajectories of the eddies within the train are assumed to be identical. Estimation of transport along the wall due to the eddy–wall encounter will now be discussed.

a. The double-frontal current

We use a zonal geostrophic double-frontal current (Fig. 6) to represent a train of eddies. The two sides of this current are asymmetrical ($|Y_4| > |Y_6|$) due to β. This important aspect results in a net westward transport, reproducing the same transport as that of the eddy train. For analytical tractability, we consider the eddies and the DFC to have zero potential vorticity ($\xi = 0$). Taking into account the above considerations, the equations for the zonal velocity (u^*_{zc}) and depth (h^*_{zc}) of the zonal geostrophic DFC are obtained from the system:

$$\xi = \frac{f_0 + \beta(Y - Y_0) - \partial u^*_{\mathrm{zc}} / \partial Y}{h^*_{\mathrm{zc}}} = 0 \qquad\qquad f u^*_{\mathrm{zc}} = -g' \frac{\partial h^*_{\mathrm{zc}}}{\partial Y} \; .$$

Assuming $Y_0 = 0$ and the boundary conditions $u^*_{\mathrm{zc}} = 0$ and $h^*_{\mathrm{zc}} = H_{\mathrm{zc}}$ at $Y = 0$, this system's solution is:

$$u^*_{\mathrm{zc}} = f_0 Y + \beta Y^2 / 2 \qquad (12a)$$

$$h^*_{\mathrm{zc}} = H_{\mathrm{zc}} - f_0^2 Y^2 / 2g' - f_0 \beta Y^3 / 2g' - \beta^2 Y^4 / 8g' \; . \qquad (12b)$$

b. The encounter

A zonal double-frontal current has a westward flow in its northern section and a weaker, eastward flow in its southern section. This current collides with the wall and subsequently “splits.” In this subsection, the equations that describe this interaction will be derived. It will be demonstrated here that a stationary eddy (SE) is required in the interaction area because its β-induced force is necessary to balance the other forces acting parallel to the wall.

1) MERIDIONAL WALL ($\theta = 0°$)

Fig. 7 shows a plan view of the DFC–wall encounter. The meridional limits of the domain are y_N and y_S. A northward wall-parallel flow (NC), which crosses section CD with the same net transport as the DFC, results from the interaction. A southward wall-parallel flow, crossing section AB, is topologically impossible because a current (leak) of finite cross-sectional area perpendicular to the wall cannot be achieved under conditions of poleward flow.

Applying Eq. (10) to this scenario and considering $y = Y$ (i.e., $\theta = 0°$) gives

$$-\int_C^D \left[hv^2 + g'h^2/2 - (f_0 + \beta y)\psi\right]dx + \iint_S \beta\psi\, dx\, dy = 0 \quad . \tag{13}$$

The relationship between the terms $g'h^2/2$ and $(f_0+\beta y)\psi$ will now be examined. Assuming the DFC is geostrophic when $x \to \infty$, its flow along the eastern section obeys the following relation:

$$(f_0 + \beta y)\psi\Big|_{y_S}^{y_N} - \beta\int_{y_S}^{y_N} \psi dy = g'h^2/2\Big|_{y_S}^{y_N} . \tag{14}$$

Following Arruda et al. (2004), it is assumed that $\psi = \psi_\infty(y)$ and $h = h_\infty(y)$ when $x \to \infty$. Because the current thickness at the DFC fronts is zero and $\psi_\infty = 0$ on the southern side of the current, Eq. (14) becomes

$$(f_0 + \beta y)\psi_\infty\Big|_{y_N} = \beta\int_{y_S}^{y_N} \psi_\infty dy . \tag{15}$$

Assuming now that the northward current is also geostrophic, it obeys the relation

$$(f_0 + \beta y)\psi + K = g'h^2/2 \quad , \tag{16}$$

where K is a constant of integration to be determined. This equation is also valid at point $C(\infty, y_N)$ of the domain where $h = 0$. Taking this finding into consideration and returning to Eq. (15), K is given as

$$K = -\beta\int_{y_S}^{y_N} \psi_\infty dy . \tag{17}$$

With Eqs. (13), (16), and (17), the final integrated meridional momentum equation for the domain ABCDA (Fig. 7) is given by

$$\int_0^{L_{\mathrm{nc}}} hv^2\,dx + \beta \iint_S (\psi - \psi_\infty)\,dx\,dy = 0 \quad ,$$

(18)

where L_{nc} is the width of the northward current (NC). This expression is similar to expressions presented in Arruda et al. (2004). The equation's first term represents a rocket force exerted in the domain by the northward current, which corresponds to the thick black NC arrow in Fig. 5 (left panel). The interpretation of the second term in Eq. (18) is not straightforward. It will be shown through scale analysis that this term corresponds to a β force exerted by a stationary eddy established inside the domain. This force corresponds to the central black arrow in Fig. 5 (left panel).

(i) Scales

It is assumed that the current width (Fig. 6) is $L^*_{\mathrm{zc}} \sim O(R_d)$, where R_d is the Rossby radius of the current: $R_d = (g'H_{\mathrm{zc}})^{1/2}/|f_0|$. The thickness, H_{zc}, defines the thickness scale for all the currents of the domain. The net transport between points 5 and 6 is zero. The transport between points 4 and 5 corresponds to the DFC net transport. The scales of h_5 and d_{45}, which are directly related to DFC net transport, will be determined next.

For the meridional balance equation (i.e., for the region between points 5 and 6), we can write

$$g'h_5^2/2 + \beta \int_6^5 \psi\,dy = 0\,. \tag{19}$$

In this equation, we have considered that $\psi_5 = \psi_6 = 0$ and $h_6 = 0$. The assumed DFC scales are given by $h \sim O(H_{\mathrm{zc}})$, $y \sim O(R_d)$, $u \sim O(g'H_{\mathrm{zc}})^{1/2}$, and $\psi \sim O(g'H_{\mathrm{zc}}{}^2/|f_0|)$. The parameter $\varepsilon = \beta R_d/|f_0|$, where $\varepsilon \ll 1$, defines the ratio between the variation of the Coriolis parameter along the DFC meridional width and the parameter f_0 itself (by definition, ε is zero on an f plane). With these considerations, it is possible to investigate the scales of the variables in Eq. (19):

$$[h_5] \sim O(\varepsilon^{1/2} H_{\mathrm{zc}})\,. \tag{20}$$

Assuming that the zonal velocity is constant along section 4–5, it is noted that $\partial h/\partial y \approx h_5/d_{45}$. The distance d_{45} is small, and $h_4 = 0$. Using the geostrophic relation and Eq. (20), we find that

$$[d_{45}] \sim O(\varepsilon^{1/2} R_d)\,. \tag{21}$$

The scales of the terms in Eq. (18) will now be investigated. We assume, a priori, the existence of a stationary eddy inside the domain [with a maximum depth of H_{se} and a transport function ψ_{se}, where $\psi_{\mathrm{se}} \sim O(g' H_{\mathrm{se}}^2/|f_0|)$]; we will subsequently show that the existence of this feature is necessary. The eddy's Rossby radius is given by $R_{de} = (g' H_{\mathrm{se}})^{1/2}/|f_0|$ and $H_{\mathrm{se}}/H_{\mathrm{zc}} = (R_{de}/R_d)^2$. The zonal scales, x, of the northward current, the double-frontal current, and the stationary eddy are $O(\varepsilon^{1/2} R_d)$, $O(\ell)$, and $O(R_{de})$, respectively, where ℓ is the zonal width of the domain. The respective meridional scales are $O(\ell)$, $O(R_d)$, and $O(R_{de})$. With these scales, the first term of Eq. (18) is $O(\varepsilon g' H_{\mathrm{zc}}^2 R_d)$. The second term is zero in the stagnant ocean and in the DFC (due to the geometry of its streamlines). In the northward current and stationary-eddy regions, this term is $O(\varepsilon^{5/2} g' H_{\mathrm{zc}}^2 \ell)$ and $O(\varepsilon g' H_{\mathrm{zc}}^2 R_{de}^6/R_d^5)$, respectively. The ratios of the order of the first term of Eq. (18) and these last two orders are, respectively, $\varepsilon^{3/2}\ell/R_d$ and $(R_{de}/R_d)^6$. We see that only the second term (corresponding to the stationary eddy) is capable of balancing the first term. Eq. (18) can then be rewritten in the form

$$\int_0^{L_{\mathrm{nc}}} h_{\mathrm{nc}} v_{\mathrm{nc}}^2\, dx + \beta \iint\limits_{S_{\mathrm{se}}} \psi_{\mathrm{se}}\, dx\, dy = 0\,. \tag{22}$$

In Eq. (22), S_{se} is the surface area of the stationary eddy. This equation shows that the presence of the stationary eddy is necessary for the meridional balance of forces along the wall. In this equation, the rocket force exerted by the northward current is balanced by the β-induced force of the stationary eddy (Fig. 5, left panel). From the scaling analysis, we also conclude that $R_{de} \sim O(R_d)$. Eq. (22) confirms that the eddy is anticyclonic because its second term is always negative. A streamfunction with a negative mean value is typical of anticyclonic eddies in the Southern Hemisphere. In the following section, the various terms of Eq. (22) will be examined. The goal is to develop an analytical expression for the northward-current transport and the radius of the stationary eddy (Fig. 8).

ii) Momentum and mass transport of the northward current

The first term in Eq. (22) will now be examined. The northward current (NC) has zero potential vorticity, and its velocity v_{nc} is approximated by

$$v_{\mathrm{nc}} = v_1 - f_0 x \qquad 0 \le x \le L_{\mathrm{nc}} \tag{23a}$$

and

$$v_{\mathrm{nc}} = 0 \qquad x > L_{\mathrm{nc}} \tag{23b}$$

where v_1 is the NC velocity at the wall (point 1 in Fig. 8). By geostrophy, the current thickness h_{nc} is given by

$$h_{\mathrm{nc}} = h_1 + f_0 v_1 x / g' - f_0^2 x^2 / 2g' \quad 0 \le x \le L_{\mathrm{nc}} \tag{24a}$$

and

$$h_{\mathrm{nc}} = 0 \quad x > L_{\mathrm{nc}}\,. \tag{24b}$$

Applying the geostrophic relation again to the NC,

$$T_{\mathrm{nc}} = -g' h_1^2 / 2 f_0 \quad \rightarrow \quad h_1 = \left[-2 f_0 T_{\mathrm{nc}} / g'\right]^{1/2}, \tag{25}$$

which enables us to calculate h_1. This equation confirms that $[h_1] \sim O(\varepsilon^{1/2})$ because T_{nc}, which depends on h_5 and d_{45}, also has $O(\varepsilon)$, as shown in Eqs. (20) and (21).

Applying the Bernoulli relationship between points 1 and 5 yields the velocity v_1:

$$v_1 = \left[2g'(H_{zc} - h_1)\right]^{1/2} . \qquad (26)$$

The width L_{nc} is calculated assuming that the meridional velocity v is constant along this width, which is plausible because the current is notably narrow. Taking $\partial h/\partial x = \Delta h/\Delta x$ and $v = v_1$ = constant, the geostrophic relation enables us to derive an expression for L_{nc}:

$$L_{nc} = -\frac{g' h_1}{f_0\left[2g'(H_{zc} - h_1)\right]^{1/2}} . \qquad (27)$$

These expressions for h_1, v_1, and L_{nc} depend only on the known parameters of the DFC. Using Eqs. (23) and (24), the first term of Eq. (22), the momentum M_{nc}, can now be determined:

$$M_{nc} = \int_0^{L_{nc}} h_{nc} v_{nc}^2 \, dx = h_1 v_1^2 L_{nc} + f_0 v_1^3 L_{nc}^2 / 2g' .$$

(28)

Integration of $h_{nc}v_{nc}$ between points 1 and 2 (Fig. 8) yields

$$T_{nc} = \int_0^{L_{nc}} h_{nc} v_{nc} \, dx = h_1 v_1 L_{nc} + f_0 v_1^2 L_{nc}^2 / 2g' . \qquad (29)$$

With the introduction of Eqs. (25–27) into Eqs. (28) and (29), the momentum and transport of the meridional current can now be calculated.

(iii) Momentum and radius of the stationary eddy

The second term of Eq. (22) will now be analyzed. An expression for the transport function ψ_{se} of the stationary eddy can be developed from

$$\partial \psi_{se} / \partial r = v_{\theta} h_{se} , \qquad (30)$$

where r is a cylindrical coordinate, $h_{se}(r)$ is eddy thickness (Fig. 9), and $v_\theta(r)$ is the eddy's tangential velocity. The current around the eddy also contributes to its momentum but has an order higher than ε and can therefore be neglected. The velocity and thickness profiles of a symmetrical, lens-like eddy of zero potential vorticity are given by

$$v_{\theta} = -f_0 r/2 \tag{31a}$$

$$h_{se} = f_0^2 (r_0^2 - r^2)/8g' . \tag{31b}$$

In Eq. (31b), r_0 is the radius measured from the center of the eddy to its edge (i.e., where $h_{se} = 0$). Using Eq. (31), the solution of Eq. (30) is given by

$$\psi_{se} = k + \frac{f_0^3 (r_0^2 - r^2)^2}{64 g'} , \tag{32}$$

where k is a constant of integration to be determined.

Eq. (31b) gives

$$R = \left[\frac{8g'(H_{se} - h_i)}{f_0^2} \right]^{1/2} . \tag{33}$$

Considering that $\psi_{se} = 0$ when $r = R$ and combining that with Eq. (33), we obtain $k = -g' h_i / f_0$. From the latter expression, Eq. (32) becomes

$$\psi_{se} = \frac{f_0^3 (r_0^2 - r^2)^2}{64 g'} - \frac{g' h_i^2}{f_0} \qquad r \le R . \tag{34}$$

The relation $H_{se} / H_{zc} = (R_{de} / R_d)^2$, in combination with the fact that $R_{de} \sim O(R_d)$, allows us to conclude that $H_{se} \sim O(H_{zc})$ and consequently $H_{se} >> h_i$ and $R \simeq r_0$. Thus, the second term of Eq. (22), the stationary eddy momentum M_{se}, can be written as

$$M_{se} = \beta \iint_{S_{se}} \psi_{se} \, dx \, dy = \frac{f_0^3 \beta}{2^7 (3) g'} \int_0^{2\pi} R^6 d\theta = \frac{\pi f_0^3 \beta R^6}{2^6 (3) g'} , \tag{35}$$

where the term with an order higher than ε was neglected. From Eq. (22) with Eqs. (28) and (35), the radius of the SE is found to be

$$R = 2\left\{-\left[\frac{3g'}{\pi f_0^3 \beta}\right]\left[h_1 v_1^2 L_{\mathrm{nc}} + \frac{f_0 v_1^3 L_{\mathrm{nc}}^2}{2g'}\right]\right\}^{1/6} . \qquad (36)$$

The principal variables associated with the stationary eddy are shown in Fig. 9.

2) TILTED WALL ($\theta > 0$º)

Fig. 10 shows the case of a double-frontal current that splits at a tilted wall. Again, a stationary eddy is required for the momentum balance to hold. Applying to Eq. (10) the same procedure used in the prior subsection results in

$$\sin\theta \int_{Y_6}^{Y_4} h^*(u^*)^2 \, dY + \int_0^{L_{\mathrm{nc}}} hv^2 \, dx + \beta\cos\theta \iint_S \psi \, dx \, dy = 0 .$$

(37)

Compared to Eq. (22), Eq. (37) has an extra term (the first term), which corresponds to the wall-parallel component of the zonal force exerted in the domain by the DFC (see the WC-force black arrow shown in Fig. 5, left panel). The last term of Eq. (37) also represents a component parallel to the wall—the β-induced force of the SE. When $\theta = 0°$, Eq. (37) reduces to Eq. (22) as expected.

(i) Scales

The orders of the three terms of Eq. (37) are, left to right, $\sim O[g' H_{\mathrm{zc}}^2 R_d \sin\theta]$, $\sim O(\varepsilon g' H_{\mathrm{zc}}^2 R_d)$, and $\sim O[\varepsilon g' H_{\mathrm{zc}}^2 R_{de}(R_{de}/R_d)^5 \cos\theta]$. Two scenarios are possible. The first scenario occurs when $\sin\theta \sim O(\varepsilon)$, which produces three terms in Eq. (37) with the same $\sim O(\varepsilon g' H_{\mathrm{zc}}^2 R_d)$, and again $R_{de} \sim O(R_d)$. The first two terms correspond to forces exerted in the domain (toward the southwest) by the double-frontal current and the northward current. The stationary eddy is again necessary because only its northward β-induced force is able to balance these forces. The second situation occurs when $\sin\theta >> \varepsilon$. Only the third term of Eq. (37), which is the term related to the SE, is now able to balance the first term of the expression. A new relation for R_d/R_{de} is now established:

$$R_{de} \sim O(R_d / \varepsilon^{1/6}). \tag{38}$$

Eq. (38) shows that the SE radius will be greater in this second scenario, which is to be expected because its β-induced force must now balance an extra force.

(ii) Balance of forces

The wall-parallel component of the force exerted by the DFC is given by

$$M_{\mathrm{zc}} = \sin\theta \int_{Y_6}^{Y_4} h_{\mathrm{zc}}^* (u_{\mathrm{zc}}^*)^2 dY = \sin\theta \left[\frac{f_0^2 H_{\mathrm{zc}} (Y_4^3 - Y_6^3)}{3} + \frac{f_0 \beta H_{\mathrm{zc}} (Y_4^4 - Y_6^4)}{4} - \frac{f_0^4 (Y_4^5 - Y_6^5)}{10 g'} - \frac{f_0^3 \beta (Y_4^6 - Y_6^6)}{6 g'} \right]. \tag{39}$$

The coordinates Y_4 and Y_6 indicate the position of the DFC fronts. They are calculated by applying Eq. (12) in the points (h_{zc}^*, Y) given by $(0, Y_4)$ and $(0, Y_6)$. The third equation is $T_{\mathrm{zc}} = \int_{Y_6}^{Y_4} h_{\mathrm{zc}}^* u_{\mathrm{zc}}^* dY$. The resulting system of three equations has three unknowns (Y_4, Y_6, and H_{zc}), as expected. Eqs. (28) and (35) are still valid for the second and third terms of Eq. (37). Taking these considerations into account, the final expression for the balance of forces along the wall is

$$\sin\theta \left[\frac{f_0^2 H_{\mathrm{zc}} (Y_4^3 - Y_6^3)}{3} + \frac{f_0 \beta H_{\mathrm{zc}} (Y_4^4 - Y_6^4)}{4} - \frac{f_0^4 (Y_4^5 - Y_6^5)}{10 g'} - \frac{f_0^3 \beta (Y_4^6 - Y_6^6)}{6 g'} \right] + h_1 v_1^2 L_{\mathrm{nc}} + \frac{f_0 v_1^3 L_{\mathrm{nc}}^2}{2 g'} + \frac{\pi f_0^3 \beta R^6 \cos\theta}{2^6 (3) g'} = 0 . \tag{40}$$

(iii) Radius of the stationary eddy

From Eqs. (39) and (40), the radius of the stationary eddy (Fig. 9) is given by

$$R = 2\left\{-\left[\frac{3g'}{\pi f_0^3 \beta \cos\theta}\right]\left[M_{\mathrm{zc}} + h_1 v_1^2 L_{\mathrm{nc}} + \frac{f_0 v_1^3 L_{\mathrm{nc}}^2}{2g'}\right]\right\}^{1/6}. \tag{41}$$

With $\theta = 0°$, Eq. (41) reduces to Eq. (36).

As mentioned, we considered two different scenarios for eddy train–wall interactions: a meridional wall and a tilted wall. The meridional balance is different in each case. In the first scenario, the rocket force exerted by the northward current (i.e., through leakage) is balanced by the β-induced force of the stationary eddy. In the second scenario, there is an additional force. Now the wall-parallel component of the β-induced force balances the sum of two southwestward forces—the rocket force of the northward current plus the force exerted in the domain by the wall-parallel component of the double-frontal current (Fig. 5, left panel). Hence the radius of the stationary eddy must be greater in this latter scenario. The scale analysis revealed that the presence of a stationary eddy is necessary in the interaction region because only its β-induced force can balance the other meridional forces acting along the wall.

5. Numerical Simulations

To further examine the validity of the analytical model developed here, we performed quantitative experiments using a modified version of the Bleck and Boudra reduced gravity isopycnal model (a general description of this numerical model is presented in Shi and Nof 1994). The Orlansky (1976) second-order radiation condition was applied to the open northern, southern, and eastern domain boundaries.

a. Eddy-train generation

We performed two types of experiments with respect to eddy-train generation (Table 1). In the first set of experiments (Group A), eddies were created with the “eddy cannon” introduced in Pichevin and Nof (1996). In the second set of experiments (Group B), features were specified analytically within the domain with Eq. (31). To accelerate the experiments and reduce the effect of friction, we introduced an artificially magnified value for β. To verify that the magnified β did not produce significant unwanted variation in our results, several experiments (not shown in Table 1) were also performed with the typical β. From these comparisons, we concluded that the model results were not altered by the magnified β.

Fig. 11 illustrates the model ocean and eddy cannon used for the Group A experiments. First, we suppose an imaginary domain around the "cape" (represented by the solid black horizontal line on the ocean's east side). A westward current is imposed on the northern side of the cape. Due to the small radius of curvature at the cape's tip, the current turns back on itself and returns eastward along the cape's southern boundary. At the tip of the cape, eddies are created because the flow-force (directed to the west) associated with the current entering and exiting the domain needs to be balanced. The drifting eddies exert a force (to the east) as they move westward. These eddies are similar to bullets fired from a cannon, which is why this model scenario (cape + current + eddies) has been called an "eddy cannon" (Pichevin and Nof 1999).

b. Experiments

Approximately a dozen different numerical experiments were performed, and we present here three specific examples that are generally representative of the results (Table 1). The first (Case AI) and third (Case BIII) scenarios, with a meridional wall in the domain, correspond directly to our theoretical calculations. In the first case, large eddies were generated with the eddy cannon; in the third case, smaller eddies were created analytically.

The second scenario (Case AII) had a tilted wall, which corresponds more directly to a typical oceanic situation. In all of the experiments, the streamlines were not disturbed when the fluid left the domain, suggesting that the radiation boundary conditions used in the open boundaries were appropriate. To allow for sufficient resolution within the leaks, we worked with relatively large eddies (h ~ 3000 m). The viscosity (400 m^2 s^{-1}) may seem large; however, this value is acceptable in this context because of the coarse spatial resolution and large meridional grid size (Table 1), which imply acceptably small diffusion speeds (0.5 cm s^{-1}).

c. Numerical results

In the first scenario (Case AI), the domain had a meridional wall on its western side, and a train of large eddies was generated with the eddy cannon. In the representative example (Exp. AI02, Table 1), a zero-potential-vorticity run was conducted with domain dimensions of 1600 x 950 km and a β of 8.10^{-11} $m^{-1}s^{-1}$ (approximately four times greater than the typical β). The runtime was four years, and an eddy of radius ~240 km was generated every 112 days. Fig. 11 shows the first eddy (E_1) colliding with the meridional wall and a second eddy (E_2) nearly pinched off from the eddy cannon. Transports were calculated for sections A, B, and C. The transport of the eddy train was 27 Sv. Fig. 12 shows the stationary eddy created in the domain. Time-averaged depth (upper-layer thickness) and velocity at each grid point were used to identify the eddy boundary and calculate eddy size. The stationary eddy shown in Fig. 12 has a radius of approximately 115 km.

For model verification, we compared the dimensions of features common to the analytical and numerical models. In the analytical model, the double-frontal current had a maximum depth H_{zc} of 2877 m, a width L^*_{zc} of 152 km, and an R_d of 54 km. From Eq. (25), h_1 (vertical thickness of the northward current at point 1; Fig. 8) is 737 m. In the corresponding numerical model, this depth (measured at section A, Fig. 11) was 670 m; giving a value of 1.1 for the ratio of the analytical and numerical values. The SE radius, according to Eq. (36), was 105 km, yielding a ratio of 0.91 for the analytically and numerically determined radii. Thus, the analytical and numerical results are in excellent agreement.

In the second scenario (Case AII), eddies were again generated with an eddy cannon but the wall in this case was tilted 23º. The model parameters mentioned above were retained, but the zonal dimension of the domain was increased slightly to maintain an approximately constant time for eddy transit from the cannon to the wall. Comparison of the first and second scenarios is useful for evaluating the effects of a DFC with a linear momentum different from that of the eddy train. The experiment representative of the tilted-wall scenario (Exp. AII04, Table 1) resulted in a stationary-eddy radius of 130 km, while the analytical result, calculated from Eq. (41), was 154 km—a greater difference (ratio ~ 1.2) than was observed for the first scenario (ratio ~ 0.91). The greater difference between the analytical and numerical Case II SE radii can be attributed to the greater difference in linear momentum of the DFC versus the eddy train. In this second scenario, $\sin\theta >> \varepsilon$, and Eq. (37), where the term $\varepsilon^{-1/6}$ is 1.7, must be applied. The ratio of the analytical radii of the second and first scenarios was 154/105 ~ 1.5, which is consistent with the magnitude of the $\varepsilon^{-1/6}$ term in the tilted-wall case.

Other experiments were performed for a range of wall-tilt angles between 0º and 40º (Table 1; Fig. 13). The difference between the analytical and numerical results increased as wall tilt increased. At $\theta = 40º$, the ratio of the analytically obtained stationary-eddy radius to the numerically calculated radius was 1.2; for lower values of θ, the ratios were closer to 1. The greater differences between the analytical and numerical model results at higher angles of wall tilt are due to the increasing influence of the DFC linear momentum as θ increases.

In the third scenario (Case BIII), a train of small to medium eddies was generated analytically within a domain with a meridional wall on its western side. Comparison of the first and third scenarios allows for an evaluation of the sensitivity of the analytical model to eddy size. The grid was given a higher resolution to accommodate the smaller width of the leak. For the representative case (Exp. BIII04), the impinging eddies had radii ~ 117 km, and the transport of the train of eddies was 0.54 Sv. The northward-current vertical thickness h_1, obtained from Eq. (25), was 104 m, whereas in the numerical model it was 90 m (ratio ~ 1.2). The analytical SE radius obtained from Eq. (36) was 56 km, and the numerically calculated radius was 70 km (ratio ~ 0.8). The eddy had an analytical radius of deformation of ~20 km, which was equivalent to the DFC ~ $O(R_d)$. Additional experiments with different impinging-eddy dimensions were performed, and the resulting differences between the analytical and numerical SE radii were always <30% (this maximum value was obtained for impinging eddies of radii ~65 km). The smaller the impinging eddies, the greater the difference between the analytical and numerical results. As will be discussed below, this pattern can be attributed to the influence of the centrifugal force of the eddies.

We conclude from these comparisons that the numerical experiments clearly support the theoretical calculations. The model results and their implications are discussed in more detail in the next section.

6. Discussion and Conclusions

We analytically investigated an encounter between a train of highly nonlinear lens-like eddies (represented by a geostrophic double-frontal current) and a continental boundary (represented by a vertical wall). The accompanying numerical experiments (Table 1) were performed with the objective of validating the analytical model. The thickness, width, and transport of the northward current along the wall (i.e., the leak from the interiors of the eddies, generated after eddy–wall contact) and the radius of the stationary eddy were calculated with the formulas proposed here. These quantities are provided by Eqs. (24), (27), (29), and (36), respectively, with the aid of Eqs. (25) and (26). The SE radius for any scenario with a tilted wall is given by Eq. (41).

The geostrophic double-frontal current (DFC) has the same transport and potential vorticity (assumed to be zero) as the train of eddies upstream of the collision zone (see Figs. 6, 8). However, there are some limitations involved in the use of this current as an analytical analogue of a train of eddies. The mass and vorticity can be matched, but the DFC cannot possibly have the same energy and momentum as the train, as this circumstance would overconstrain the system. Experiments within the second numerical scenario (Case AII) showed that differences between the analytical and numerical model results increase with increasing wall tilt—i.e., when a component of the DFC momentum is included in the momentum balance along the wall. The maximum difference was 22% (observed with a wall tilt of 40^{o}; Fig. 13), which, though greater than the difference for a meridional wall (Case AI), is still acceptable. Using the Brazilian continental margin as an example of an area where collisions between anticyclonic rings and a continental boundary seem inevitable, a typical wall tilt would be approximately 30°, which produces a difference of approximately 20% between the analytical and numerical results (Fig. 13). Agulhas eddies typically approach the South American continental boundary near 28ºS (Fig. 1B), where the boundary has a nearly north–south orientation ($\theta \sim 0°$), a condition for which the analytical and numerical model results are in best agreement.

We also assumed that the DFC is in geostrophic balance, but the centrifugal force in the eddy interior does not allow movement of the DFC to be purely geostrophic. As a result, the DFC thicknesses and velocities will differ from those of the eddies in the train, with deviations directly proportional to the Rossby number of the eddies (Flierl 1979). Experiments within the third (Case BIII) scenario demonstrated that differences between the analytical and numerical model results depend inversely on eddy radius. With large eddies, which have small centrifugal force, the analogous DFC more convincingly reproduces the train of eddies, and similarities between the models are more evident. Accordingly, in the first scenario (Case AI, a train of large eddies), the difference between the analytical and numerical models was small.

We conclude:

(i) The presence of a stationary eddy is necessary in the double-frontal current–wall contact zone (Figs. 9, 12) because only its β-induced force is able to balance the other forces acting along the wall, as shown by Eqs. (22) and (37). The SE radius is directly proportional to (a) the transport of the train of eddies, (b) the tilt of the wall, and (c) the density difference between the eddy interior fluid and the surrounding fluid [as shown by Eqs. (36) and (41)]. The eddy radius is inversely proportional to the latitude of the contact zone.

(ii) After contact with the wall, the impinging eddies leak their interior fluid toward the equator (Fig. 11), thus creating a northward current along the wall with the same transport as that of the impinging eddy train (or with the same net transport of the double-frontal current).

(iii) Eq. (37) shows that the encounter of an eddy train with a wall corresponds to a balance among three forces along the wall: the poleward component of the zonal force that is exerted in the domain by the double-frontal current, the poleward rocket force that results from the leak, and the equatorward component of the β-induced force of the stationary eddy.

(iv) The numerical model results are in good agreement with the analytical solution.

Our results are applicable to encounters between Agulhas rings and the Brazilian continental boundary and its western boundary current, the Brazil Current (Figs. 1, 2). Such encounters have not been directly documented in situ, but indirect evidence indicates they are likely inevitable. For example, altimetry observations have tracked Agulhas eddies that crossed the South Atlantic Ocean and closely approached the South American continent (Fig. 1A). We calculated the radii of the ten eddies observed to have made this transoceanic journey between 1998 and 2006 (Fig. 1A). Eddy radius at the western terminus of each trajectory was calculated as the radius of a circle with an area equal to that enclosed by the contour of maximum circum-average speed (Chelton et al. 2011). These westernmost eddy radii ranged from 51 to 145 km (Fig. 1B).

Assuming that all eddies are lenses and that any eddy that reaches 38.5ºW will also reach the continental boundary, it is possible to estimate the equivalent eddy train that corresponds to the sequence of ten eddies displayed in Fig. 1B. The following assumptions were also considered for this equivalent eddy train (ET): (i) the time interval T_{et} between identical successive eddies is calculated by $T_{\mathrm{et}} = \left[\sum_{i=1}^{9}(time_{i+1} - time_i)\right]/9$, where $time_i$ is measured when the i^{th} successive trajectory reaches 38.5ºW; (ii) the radius of the identical eddies (R_{et}) is the weighted radius obtained from $R_{\mathrm{et}} = \left[\sum_{i=1}^{10} R_{Ti} D_i\right] / \sum_{i=1}^{10} D_i$, where D_i is the length of the i^{th} trajectory (measured west of 38.5ºW) and R_{Ti} is the mean eddy radius of the i^{th} trajectory (calculated west of 38.5ºW); and (iii) the translation velocity of the eddies, V_{et}, is the weighted velocity obtained from the mean velocity V_{Ti} of the i^{th} trajectory and is calculated similarly to radius R_{et}. Each mean velocity V_{Ti} is calculated by $V_{Ti} = D_i/time_i$.

With the above assumptions, the resulting equivalent eddy train would have successive identical eddies with radii of 85 km, each moving westward at 5.4 cm s^{-1} and separated by a uniform distance of ~1500 km. The time interval between eddies would be 322 days (i.e., approximately one eddy per year would collide with the South American continental boundary). The resulting eddy-train transport is approximately 0.17 Sv. Using Eqs. (12), (25–27), and (36) for the case of a meridional wall yields a narrow northward current (leakage) with a width of 2.6 km and a stationary eddy with a radius of 60 km. Currently, it would be difficult to observe such an eddy from satellites, primarily because the altimetry data lack the requisite resolution. However, a stationary eddy could appear in the form of a recirculation cell embedded within the BC, thus offering a potential avenue for future research.

During the 16-year period covered by the Chelton et al. (2011) dataset, many eddies were pinched off from the retroflection zone of the Agulhas Current, but only ten were observed to cross the South Atlantic Ocean. (The other eddies could have met a variety of fates, perhaps drifting northward, advected by the Benguela Current, or perhaps splitting into other eddies or simply decaying, partially or totally.) Other types of eddies generated by other mechanisms—for example, eddies shed by the Brazil Current meanders—might also impinge on the South American continental boundary. In this work, we focus on Agulhas rings because they are much larger than the other rings and are therefore more easily observed from space and are likely have a greater effect on boundary-current processes upon collision.

We have considered only eddy–wall interactions in the absence of a swift western boundary current. However, it is reasonable to assume that the presence of the Brazil Current is important to the process because its cross-shore scale has roughly the same Rossby radius as the impinging eddies. Therefore, at least part of the signal of the impinging eddy train may become embedded in the current, thus being carried away from the collision area. In fact, propagation of sea level anomalies has been previously documented in some Southern Hemisphere western boundary currents, such as the East Australian Current (Bowen et al. 2005; Mata et al. 2006) and the Brazil Current (Campos 2006). Future studies are needed to investigate further the dynamics associated with interactions between eddies and western boundary currents.

Finally, the eddy–wall interaction model developed here suggests that the Brazil Current transport is weakened upstream from (north of) the collision zone, while its downstream transport (south of the collision zone) remains unaltered. Unfortunately, in keeping with most

Southern Hemisphere oceanic features, the current remains undersampled despite its regional and local importance. Therefore, it is not possible at this time to directly compare our results to observed transport values. Our results can be used, however, to support the development of future field experiments, which can in turn provide data to help evaluate the theory proposed here. Yet another intriguing aspect of eddy–wall interactions is the influence of eddy collisions on boundary current variability, locally as well as upstream and downstream from the collision zone. These effects can be investigated using our proposed model by replacing the continuous events modeled here with "burst" events—i.e., impingement of distinct trains consisting of several eddies each, with each train separated by periods of quiescence.

Acknowledgments. This article is a contribution to the SOS-CLIMATE project (CNPq/MCT/PROANTAR: 520189/2006-0), which receives support from the Conselho Nacional de Desenvolvimento Científico e Tecnológico (CNPq), Ministério da Ciência e Tecnologia (MCT), and Programa Antártico Brasileiro (PROANTAR). It is also a contribution to the MOVAR Project (CNPq/Universal-2008:474057/2008-9), which receives support from the CNPq. José L. L. Azevedo acknowledges funding received from the Coordenação de Aperfeiçoamento de Pessoal de Nível Superior (CAPES, BEX 2097.07-9) and the Inter-American Institute for Global Change Research (IAI/CRN 2076), which receives support from the U.S. National Science Foundation (NSF Grant GRO-0452325). M. M. Mata acknowledges support received from CNPq (Pq-2: 307630/2009-9). D. Nof's research is supported by NSF grants #OCE-0752225 and #ARC-0902835 as well as a Binational Science Foundation grant (#2006296). The authors thank the anonymous reviewers for their valuable comments.

APPENDIX

List of Symbols

d_{45}	distance between points 4 and 5 of the double-frontal current (Figs. 6, 8)
D_i	length of the westernmost (west of 38.5°W) segment of the i^{th} eddy trajectory of the Chelton et al. (2011) data subset (Fig. 1B)
$\mathrm{D_o}$	model domain (Fig. 4)
f	Coriolis parameter [defined by $f = f_0 + \beta(Y - Y_0)$]
f_0	Coriolis parameter at the central meridional coordinate (latitude) Y_0 of the domain
g	gravity
g'	reduced gravity [$g' = (\Delta\rho/\rho)g$]
h	depth in an xy Cartesian system
h^*	depth in an XY Cartesian system
h_i	depth at the interface between the stationary eddy and the surrounding current (see Fig. 9)
h_nc	depth (vertical thickness) of the northward current
h_se	depth (vertical thickness) of the stationary eddy (Fig. 9)
h^*_zc	depth (vertical thickness) of the zonal current (or DFC) in an XY Cartesian system
h_∞	depth (vertical thickness) of the zonal current (or DFC) when $x \rightarrow \infty$
$h_{1,2...}$	depth (vertical thickness) at point 1, 2 ... (Fig. 8)
H_se	maximum depth of the stationary eddy (Fig. 9)
H_zc	maximum depth of the zonal current (or DFC)
k, K	integration constants
ℓ	zonal dimension (width) of the domain
L_nc	width of the northward current (Fig. 8)

L^*_{zc}	width of the zonal current (or DFC) in an *XY* Cartesian system (Figs. 6, 8)
M_{nc}	momentum of the northward current
M_{se}	momentum of the stationary eddy
M_{zc}	momentum of the zonal current (or DFC)
r	cylindrical coordinate (radius)
r_0	stationary eddy radius (Fig. 9), as measured from the eddy center to the eddy border (where h_{se}=0)
R	stationary eddy radius (Fig. 9), as measured from the eddy center to the eddy's interface with the surrounding current (where $h_{se}=h_i$)
R_d	Rossby deformation radius of the zonal current (or DFC)
R_{de}	Rossby deformation radius of the stationary eddy
R_{et}	radius of individual eddies in the analytical eddy train that corresponds to the ten eddies of the Chelton et al. (2011) data subset (see Fig. 1B)
R_o	Rossby number
R_{Ti}	mean radius of the i^{th} Chelton et al. (2011) eddy over its westernmost trajectory segment (west of 38.5°W; Fig. 1B)
S	surface area of the model domain D_o
S_{se}	surface area of the stationary eddy
$T_{BC,AB..}$	transport across sections BC and AB of the model domain (Fig. 5, right panel)
T_{et}	time interval between successive eddies of the eddy train
$time_i$	time when the i^{th} eddy reaches 38.5°W
T_{nc}	transport of the northward current
T_{zc}	transport of the zonal current (or DFC)
u	zonal component of velocity in an *xy* Cartesian system
u^*	zonal component of velocity in an *XY* Cartesian system

u^*_{zc}	zonal component of velocity of the westward current (or DFC) in an *XY* Cartesian system
v	meridional component of velocity in an *xy* Cartesian system
v^*	meridional component of velocity in an *XY* Cartesian system
V_{et}	translational velocity of the eddies in the eddy train corresponding to the Chelton et al. (2011) data subset (Fig. 1B)
v_{nc}	meridional component of velocity of the northward current (Fig. 8)
V_{Ti}	mean velocity of the i^{th} Chelton et al. (2011) eddy over its westernmost trajectory segment (west of 38.5°W; Fig. 1B)
$v_{1,2...}$	meridional component of velocity at point 1, 2, ... (Fig. 8)
v_θ	orbital (tangential) velocity of the stationary eddy
x, X	zonal coordinate in an *xy* (*XY*) Cartesian system (Fig. 4)
y, Y	meridional coordinate in an *xy* (*XY*) Cartesian system (Fig. 4)
y_N, y_S	northern and southern limits of the model domain (Figs. 7, 8, 10)
Y_0	central meridional coordinate of the model domain
$Y_{4,6}$	meridional coordinate of points 4 and 6 (Fig. 6) of the zonal current (or DFC)
β	parameter that expresses meridional variation of the Coriolis parameter [$\beta = \Delta f / \Delta Y$]
ε	parameter defined by $\varepsilon = \beta R_d / \lvert f_0 \rvert$
θ	angle between the *xy* and *XY* Cartesian systems—i.e., the angle of the wall with respect to geographic north (Fig. 4)
ϕ	boundary of the domain (Fig. 4)
ρ	density
$\Delta\rho$	density difference between fluid layers
Δt	time step
ψ	typical streamfunction (defined by $\partial\psi/\partial y = -uh$ and $\partial\psi/\partial x = vh$)

ψ_{se} streamfunction of the stationary eddy (defined by $\partial\psi_{se}/\partial r = v_\theta h_{se}$)

ψ_∞ streamfunction of the zonal current (or DFC) when $x \rightarrow \infty$

ξ potential vorticity

List of Abbreviations

BC	Brazil Current
BMCZ	Brazil–Malvinas Confluence Zone
DFC	double-frontal current
ET	eddy train
NC	current entering or exiting the northern boundary of the model domain (in the case examined here, NC always exits northward)
SC	current entering or exiting the southern boundary of the model domain (in the case examined here, SC does not exist)
SE	stationary eddy
WC	westward current
ZC	zonal current

References

Agra, C., and D. Nof, 1993: Collision and separation of boundary currents. *Deep-Sea Res.*, **40**, (11/12), 2259–2282.

Arruda, W., 2002: Eddies along western boundaries. Ph.D. dissertation, The Florida State University, 90 pp.

Arruda, W. Z., D. Nof, and J. J. O´Brien, 2004: Does the Ulleung eddy owe its existence to β and nonlinearities? *Deep-Sea Res. I*, **51**, 2073–2090.

Beal, L. M., W. P. M. De Ruijter, A. Biastoch, R. Zahn, and SCOR/WCRP/IAPSO Working Group 136, 2011: On the role of the Agulhas system in ocean circulation and climate. *Nature*, **472**, 429–436, doi: 10.1038/nature09983.

Biastoch, A., C. W. Böning, F. U. Schwarzkopf, and J. R. E. Lutjeharms, 2009: Increase in Agulhas leakage due to poleward shift of Southern Hemisphere westerlies. *Nature*, **462**, 495–498, doi: 10.1038/nature08519.

Bleck, R., and D. Boudra, 1981: Initial testing of a numerical ocean circulation model using a hybrid (quasi-isopycnic) vertical coordinate. *J. Phys. Oceanogr.*, **11**, 755–770.

Bowen, M., J. L. Wilkin, and W. J. Emery, 2005: Variability and forcing of the East Australian Current. *J. Geophys Res.*, **110**, C03019, doi:10.1029/2004JC002533.

Byrne, D. A., A. L. Gordon, and W. F. Haxby, 1995: Agulhas eddies: A synoptic view using Geosat ERM data. *J. Phys. Oceanogr.*, **25**, 902–917.

Campos, E. J. D., 2006: Equatorward translation of the Vitoria Eddy in a numerical simulation. *Geophys. Res. Lett.*, **33**, L22607, doi:10.1029/2006GL026997.

Chelton, D. B., M. G. Schlax, R. M. Samelson, and R. A. Szoeke, 2007: Global observations of large oceanic eddies. *Geophys. Res. Lett.*, **34**, L15606, doi: 10.1029/2007GL030812.

Chelton, D. B., M. G. Schlax, and R. M. Samelson, 2011: Global observations of nonlinear mesoscale eddies. *Prog. Oceanogr.*, **91**, 167–216, doi:10.1016/j.pocean.2011.01.002.

Cushman-Roisin, B., E. P. Chassignet, and B. Tang, 1990: Westward motion of mesoscale eddies. *J. Phys. Oceanogr.*, **20**, 758–768.

Duncombe Rae, C. M., 1991: Agulhas retroflection rings in the South Atlantic Ocean: An overview. *South Afr. Mar. Sci.*, **11**, 327–344.

Flierl, G. R., 1979: A simple model for a structure of warm and cold core rings. *J. Geophys. Res.*, **84,** C2, 781–785.

Garzoli, S. L., P. L. Richardson, C. M. Duncombe Rae, D. M. Fratantoni, G. J. Goni, and A. J. Roubicek, 1999: Three Agulhas rings observed during the Benguela Current Experiment. *J. Geophys. Res.*, **104,** C9, 20971–20985, doi:10.1029/1999JC900060.

Goni, G. J., S. L. Garzoli, A. J. Roubicek, D. B. Olson, and O. B. Brown, 1997: Agulhas ring dynamics from TOPEX/POSEIDON satellite altimeter data. *J. Mar. Res.,* **55,** 861–883.

Killworth, P. D., 1983: On the motion of isolated lenses on a beta-plane. *J. Phys. Oceanogr.*, **13**, 368–376.

Kundu, P. K., and I. M. Cohen, 2008: *Fluid Mechanics*, Academic Press, Elsevier, 4^{th} Ed., 878 p.

Lamb, H., 1932: *Hydrodynamics*, Cambridge University Press, Cambridge, 738 pp.

Lebedev, I., and D. Nof, 1996: The drifting confluence zone. *J. Phys. Oceanogr.*, **26**, 2429-2448.

Lebedev, I., and D. Nof, 1997: Collision of boundary currents: beyond a steady state. *Deep Sea Res.*, **44**, 771–791.

Lentini, C. A. D., D. B. Olson, and G. P. Podestá, 2002: Statistics of Brazil Current rings observed from AVHRR: 1993 to 1998. *Geophys. Res. Lett.*, **29**, doi 10.1029/2002GL015221.

Lutjeharms, J. R. E., 2010: *The Agulhas Current*, Springer-Verlag, 342 p.

Masuda, A., 1988: A skewed eddy of Batchelor-modon type. *J. Ocean. Soc. Japan*, **43**, 383–394.

Mata, M. M., S. E. Wijffels, J. A. Church, and M. Tomczak, 2006: Eddy shedding and energy conversions in the East Australian Current. *J. Geophys. Res.*, **111**, C09034, doi:10.1029/2006JC003592.

Matano, R. P., 1993: On the separation of the Brazil Current from the coast. *J. Phys. Oceanogr.*, **23**, 79–90.

McDonagh, E. L., K. J. Heywood, and M. P. Meredith, 1999: On the structure, paths, and fluxes associated with Agulhas rings. *J. Geophys. Res.*, **104**, C9, 21007–21020, doi:10.1029/1998JC900131.

Minato, S., 1982: Geostrophic adjustment near the coast. *J. Ocean. Soc. Japan*, **38**, 225–235.

Minato, S., 1983: Geostrophic response near the coast. *J. Ocean. Soc. Japan*, **39**, 141–149.

Nof, D., 1981: On the β-induced movement of isolated baroclinic eddies. *J. Phys. Oceanogr.*, **11**, 1662–1672.

Nof, D., 1983: On the migration of isolated eddies with application to Gulf Stream rings. *J. Mar. Res.*, **41**, 399–425.

Nof, D., 1988a: Draining vortices. *Geophys. Astrophys. Fluid Dyn.*, **42**, 187–208.

Nof, D., 1988b: Eddy-wall interactions. *J. Mar. Res.*, **46**, 527–555.

Nof, D., 1999: Strange encounters of eddies with walls. *J. Mar. Res.*, **57**, 739–761.

Orlanski, I., 1976: A simple boundary condition for unbounded hyperbolic flows. *J. Comput. Phys.*, **21**, 251–269.

Palma, E. D., R. P. Matano, and A. R. Piola, 2008: A numerical study of the Southwestern Atlantic Shelf circulation: Stratified ocean response to local and offshore forcing. *J. Geophys. Res.*, **113**, C11010, doi: 10.1029/2007JC004720.

Pichevin, T., and D. Nof, 1996: The eddy cannon. *Deep-Sea Res. I*, **43** (9), 1475–1507.

Pichevin, T., D. Nof, and J. Lutjeharms, 1999: Why are there Agulhas rings?. *J. Phys. Oceanogr.*, **29**, 693–707.

Saffman, P., 1979: The approach of a vortex pair to a plane surface in inviscid fluid. *J. Fluid Mech.*, **92**, 497–503.

Shi, C., and D. Nof, 1993: The splitting of eddies along boundaries. *J. Mar. Res.*, **51**, 771–795.

Shi, C., and D. Nof, 1994: The destruction of lenses and generation of wodons. *J. Phys. Oceanogr.*, **24**, 1120–1136.

Umatani, S., and T. Yamagata, 1987: Evolution of an isolated eddy near a coast and its relevance to the "Kyucho". *J. Ocean. Soc. Japan*, **43,** 197–203.

Wainer, I., P. Gent, and G. Goni, 2000: Annual cycle of the Brazil–Malvinas confluence region in the National Center for Atmospheric Research Climate System Model. *J. Geophys. Res.*, **105,** C11, 26167–26177.

Witter, D. L., and A. L. Gordon, 1999: Interannual variability of South Atlantic circulation from 4 Years of TOPEX/POSEIDON satellite altimeter observations. *J. Geophys. Res.*, **104**, 20927–20948.

Yasuda, I., K. Okuda, and K. Mizuno, 1986: Numerical study on the vortices near boundaries—considerations on warm core rings in the vicinity of east coast of Japan. *Bull. Tohoku Regional Fish. Res. Lab.*, **48**, 67–86.

TABLES

TABLE 1. Numerical model experiments and principal parameters. R_{et} is the radius of each eddy in the eddy train, θ is the angle of the tilted wall (Fig. 4), Δt is the time step, and ν is the eddy viscosity. The remaining notation is conventional and is defined in the text and appendix. All eddies had a zero potential vorticity. Experiments taken as representative examples of each case (scenario) are marked in bold.

Group	Eddy-train generation	Case	Scenario	Principal Parameters	Variations/Experiments
A	**Eddy cannon**	I	**Large eddies and a meridional wall** Grid size (x vs. y): 320 x 95 Grid resolution: 5 x 10 km Basin size: 1600 x 950 km	$\beta = 8.10^{-11}$ m^{-1} s^{-1} ν = 400 m^2 s^{-1} $f_0 = -10^{-4}$ s^{-1} $g' = 10^{-2}$ m s^{-2} Δt = 288 s	Exp. 01: R_{et} = 220 km (θ = 0°) **Exp. 02: R_{et} = 240 km (θ = 0°)** Exp. 03: R_{et} = 280 km (θ = 0°)
		II	**Large eddies and a tilted wall** For Exp. 01, 02, 03, 08, 09, and 10, grid size, grid resolution, and basin size are the same as for case I. For the other experiments, Grid size (x vs. y): 350 x 95 Grid resolution: 5 x 10 km Basin size: 1750 x 950 km	$\beta = 8.10^{-11}$ m^{-1} s^{-1} ν = 400 m^2 s^{-1} $f_0 = -10^{-4}$ s^{-1} $g' = 10^{-2}$ m s^{-2} Δt = 288 s	Exp. 01: R_{et} = 240 km (θ = 0°) Exp. 02: R_{et} = 240 km (θ = 8°) Exp. 03: R_{et} = 240 km (θ = 16°) **Exp. 04: R_{et} = 240 km (θ = 23°)** Exp. 05: R_{et} = 240 km (θ = 30°) Exp. 06: R_{et} = 240 km (θ = 35°) Exp. 07: R_{et} = 240 km (θ = 40°) Exp. 08: R_{et} = 280 km (θ = 0°) Exp. 09: R_{et} = 280 km (θ = 8°) Exp. 10: R_{et} = 280 km (θ = 16°) Exp. 11: R_{et} = 280 km (θ = 23°) Exp. 12: R_{et} = 280 km (θ = 30°) Exp. 13: R_{et} = 280 km (θ = 35°) Exp. 14: R_{et} = 280 km (θ = 40°)
B	**Analytically created within the domain**	III	**Medium and small eddies and a meridional wall** Grid size (x vs. y): 410 x 64 Grid resolution: 1 x 5 km Basin size: 410 x 320 km	$\beta = 4.10^{-11}$ m^{-1} s^{-1} ν = 200 m^2 s^{-1} $f_0 = -10^{-4}$ s^{-1} $g' = 10^{-2}$ m s^{-2} Δt = 72 s	Exp. 01: R_{et} = 65 km (θ = 0°) Exp. 02: R_{et} = 80 km (θ = 0°) Exp. 03: R_{et} = 95 km (θ = 0°) **Exp. 04: R_{et} = 117 km (θ = 0°)**

FIGURE CAPTIONS

FIG. 1. (A) Anticyclonic eddy trajectories that began near the Agulhas retroflection zone and ended west of 38.5°W, as tracked between 14 October 1992 and 31 December 2008. (B) Final eddy position and radius (km) for each trajectory. The dashed line shows the average latitude at which these eddies approach the South American continental boundary (27.9°S). The 200 m and 2000 m isobaths are shown in both figures. Eddy data are from http://cioss.coas.oregonstate.edu/eddies/ (Chelton et al. 2011).

FIG. 2. Bathymetry and western boundary currents of the Southwestern Atlantic Shelf region. The white circles represent anticyclonic eddies that originated from the Agulhas Current and are now approaching the South American boundary. Map and schematic current paths adapted from Palma et al. (2008).

FIG. 3. Forces influencing the migration of an eddy along a continental wall. The annotations *ac* and *c* indicate anticyclonic and cyclonic eddies, respectively. The zonal white arrows represent a westward eddy velocity due to β or advection. The small meridional white arrows indicate the leak of the eddy after contact with the wall. The thick meridional white arrows represent the image effect, the gray arrows represent β-induced forces, and the black arrows represent rocket forces. The net balance of these three forces determines the post-collision rate and direction of eddy migration along the wall.

FIG. 4. Plan view of domain D_o with a wall tilted at angle θ with respect to geographic north. The domain contains a zonal current that enters through the eastern boundary and two currents that enter or exit along the wall. The meridional axis of the coordinate system *XY* is aligned north–south; the meridional axis of the system *xy* is aligned with the wall. The term

$u^*(Y)$ is the velocity of the westward current. The numbers indicate the different domain boundaries ϕ; the letters indicate boundary limits.

FIG. 5. **Left panel:** Forces acting during an encounter of a westward current with a wall. The horizontal gray arrow indicates the force exerted in the domain by the westward current (WC) that enters the domain's eastern boundary. The vertical gray arrow indicates the β force due to a permanent eddy inside the domain. Both forces have wall-perpendicular (white arrows) and wall-parallel (black arrows) components. The SC and NC forces are exerted by currents entering or exiting through the southern and northern boundaries, respectively. Each wall-parallel force (black arrow) is associated with a corresponding term in Eq. (10). **Right panel:** Transports T at the boundaries of the domain. T_{BC} corresponds to the first term in Eq. (11), and T_{AB} (T_{CD}) corresponds to the second (third) term.

FIG. 6. Cross-sectional view of the double-frontal current (DFC) representing the train of eddies as defined by Eqs. (12a) and (12b). The meridional positions of the current's fronts are Y_4 and Y_6, its maximum depth is H_{zc} (at $Y = 0$), and its width is $L^*_{zc} = Y_4 - Y_6$. This current is asymmetrical ($|Y_4| > |Y_6|$) due to β, and it has the same transport and potential vorticity as the eddy train. The DFC has density ρ, and it is embedded in an infinitely deep layer of depth H (where $H >> H_{zc}$) and density $\rho+\Delta\rho$. Positions Y_4 and Y_5 delimit the zone of DFC net transport, which has width d_{45} and maximum depth h_5. These two variables are of $\sim O(\varepsilon^{1/2})$, and the net transport is of $O(\varepsilon)$. The net transport between points Y_5 and Y_6 is zero.

FIG. 7. Plan view of the encounter between a zonal double-frontal current and a meridional wall (gray rectangle). The current enters the domain through its eastern boundary (boundary BC). Leakage of the impinging eddies, which are here represented by the DFC, results from

the wall interaction and produces a northward current (NC) that exits the domain through its northern boundary (CD). The ocean is stagnant in two regions: a large area in the north and also a smaller area in the south where the transport function ψ was assumed to be zero. In these regions, the upper layer vanishes.

FIG. 8. Detailed plan view of the encounter between the double frontal-current and a meridional wall. The main scales [Eqs. (20) and (21)] are shown, as are the main velocity profiles [Eqs. (12a) and (23)] and the forces acting in the domain D_o. In this limiting scenario, the coordinate systems *xy* and *XY* are identical. For definition of terms, see text and previous figures.

FIG. 9. Cross-sectional view of the stationary eddy (SE). The shaded zone on the northern side represents the surrounding current. The radius r_0 is the total radius of the eddy, which is measured from the eddy's center to its rim (where the eddy thickness vanishes). R is the distance from the eddy's center to the eddy–current interface; the vertical dimension of the interface is h_i. Radius r is the distance from the eddy center to any location where the eddy thickness is h_{se}. The maximum thickness of the eddy is H_{se} (at the eddy center).

FIG. 10. Plan view of a double-frontal current with a tilted wall. The angle between the *xy* and *XY* coordinate systems is θ.

FIG. 11. Eddy thicknesses obtained in a representative eddy–wall numerical simulation (Case I, Exp. 02, Table 1). The contour interval is 300 m. This frame shows one eddy (E_1) contacting the western wall and leaking toward the north while a second eddy (E_2) is nearly pinched off from the eddy cannon on the right. Section A indicates where the transport of the

leak was calculated. Eddy transport was calculated as the difference between the transports across sections B and C. Numerical stability demands an eddy viscosity of 400 m^2 s^{-1} (see text for explanation); $g' = 0.01$ m s^{-2} and $f_0 = -10^{-4}$ s^{-1}. The time step is 288 sec.

FIG. 12. Eddy train (double-frontal current) thickness for one of the numerical simulations (Case I, Exp. 02, Table 1). The DFC was generated by continuous production of eddies on the right. All other model conditions are as for Fig. 11. Note the stationary eddy (SE) generated in the DFC–wall encounter region.

Fig. 13. Stationary eddy radii obtained for different angles of wall tilt (θ) with the analytical model and representative Case AII numerical experiments (Exp. 01–07, Table 1).

FIGURES

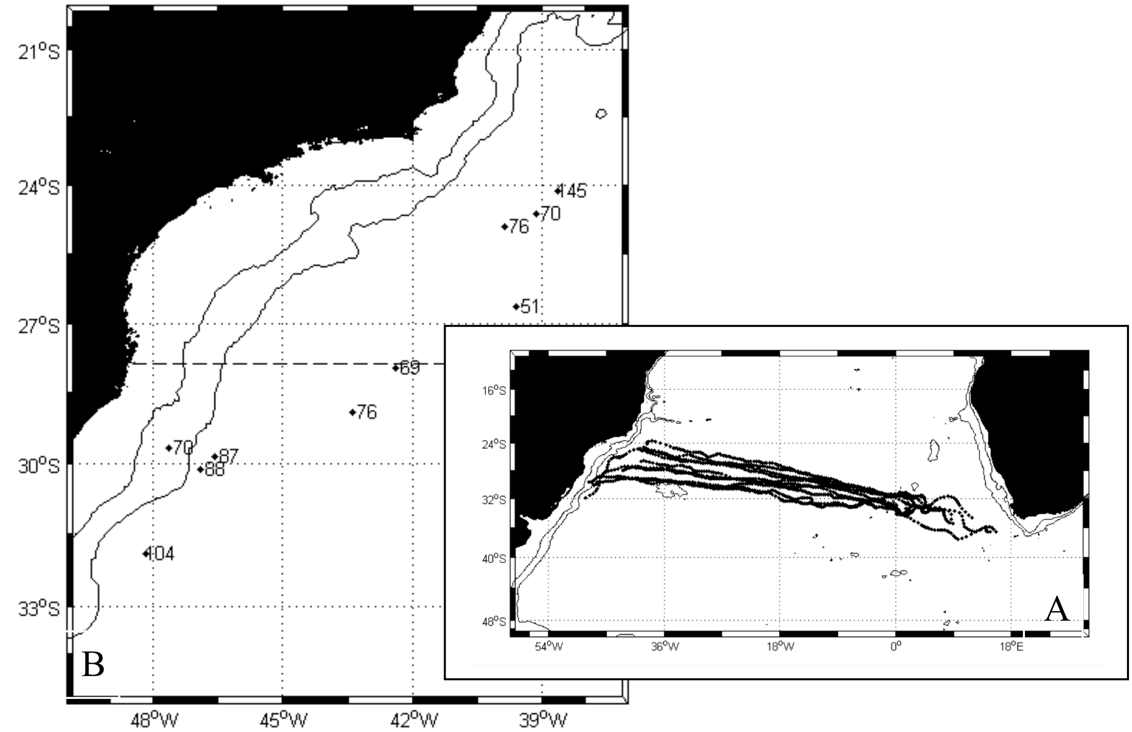

FIG. 1. (A) Anticyclonic eddy trajectories that began near the Agulhas retroflection zone and ended west of 38.5°W, as tracked between 14 October 1992 and 31 December 2008. (B) Final eddy position and radius (km) for each trajectory. The dashed line shows the average latitude at which these eddies approach the South American continental boundary (27.9°S). The 200 m and 2000 m isobaths are shown in both figures. Eddy data are from http://cioss.coas.oregonstate.edu/eddies/ (Chelton et al. 2011).

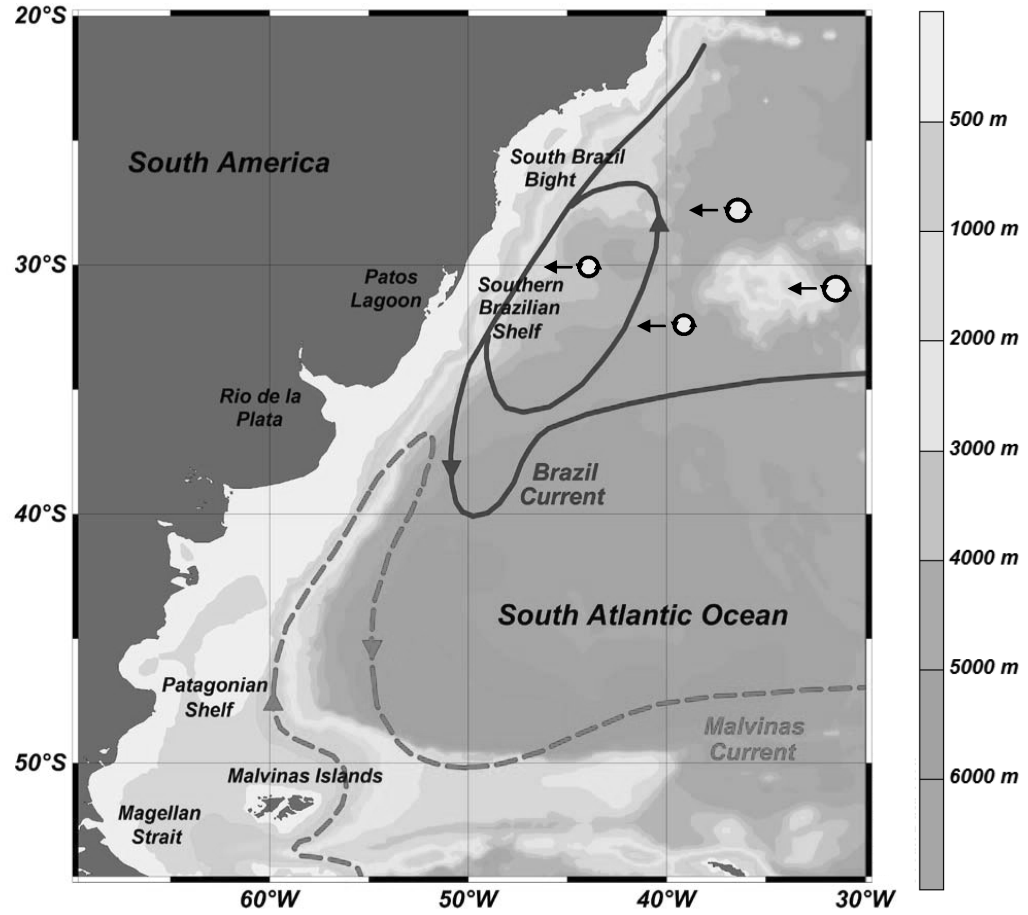

FIG. 2. Bathymetry and western boundary currents of the Southwestern Atlantic Shelf region. The white circles represent anticyclonic eddies that originated from the Agulhas Current and are now approaching the South American boundary. Map and schematic current paths adapted from Palma et al. (2008).

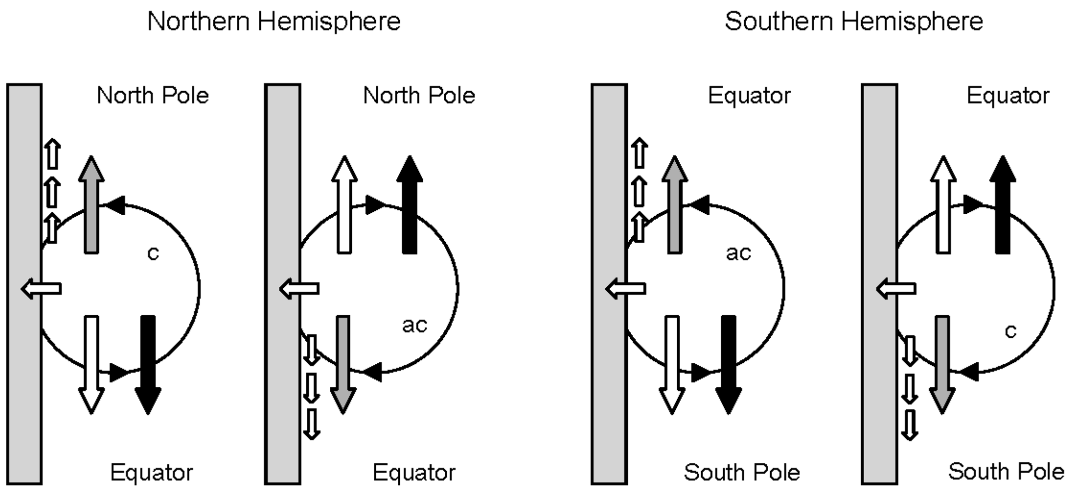

FIG. 3. Forces influencing the migration of an eddy along a continental wall. The annotations *ac* and *c* indicate anticyclonic and cyclonic eddies, respectively. The zonal white arrows represent a westward eddy velocity due to β or advection. The small meridional white arrows indicate the leak of the eddy after contact with the wall. The thick meridional white arrows represent the image effect, the gray arrows represent β-induced forces, and the black arrows represent rocket forces. The net balance of these three forces determines the post-collision rate and direction of eddy migration along the wall.

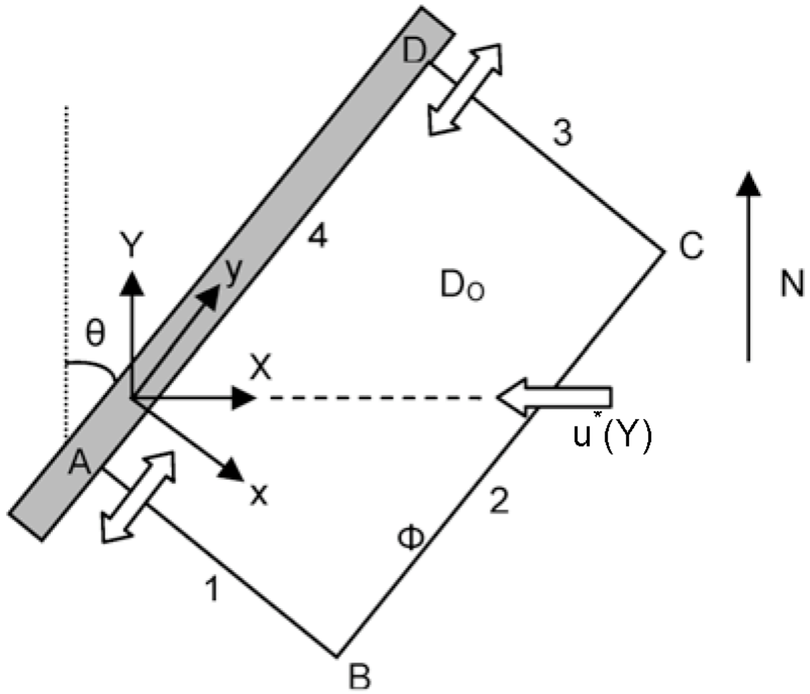

FIG. 4. Plan view of domain D_o with a wall tilted at angle θ with respect to geographic north. The domain contains a zonal current that enters through the eastern boundary and two currents that enter or exit along the wall. The meridional axis of the coordinate system *XY* is aligned north–south; the meridional axis of the system *xy* is aligned with the wall. The term $u^*(Y)$ is the velocity of the westward current. The numbers indicate the different domain boundaries ϕ; the letters indicate boundary limits.

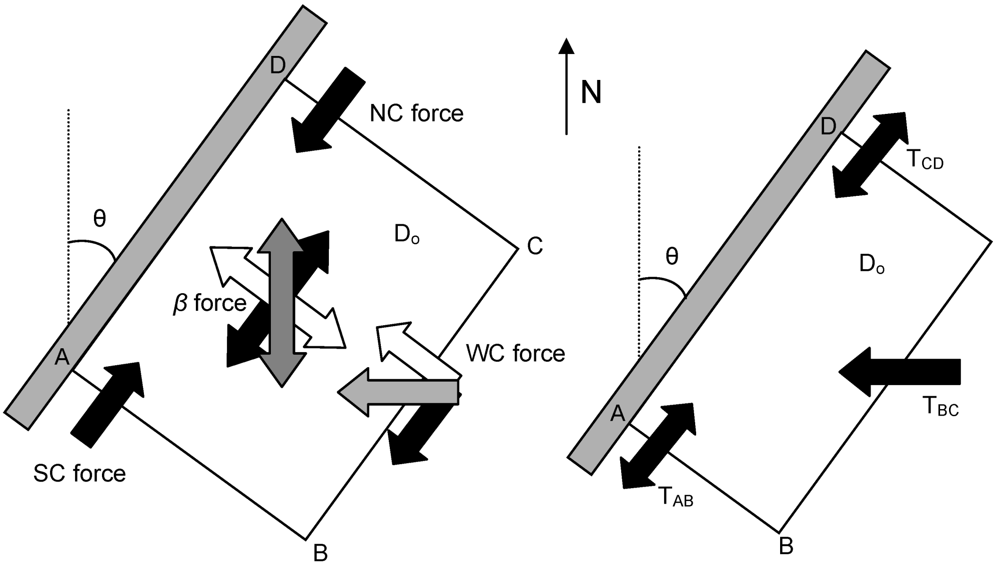

FIG. 5. **Left panel:** Forces acting during an encounter of a westward current with a wall. The horizontal gray arrow indicates the force exerted in the domain by the westward current (WC) that enters the domain's eastern boundary. The vertical gray arrow indicates the β force due to a permanent eddy inside the domain. Both forces have wall-perpendicular (white arrows) and wall-parallel (black arrows) components. The SC and NC forces are exerted by currents entering or exiting through the southern and northern boundaries, respectively. Each wall-parallel force (black arrow) is associated with a corresponding term in Eq. (10). **Right panel:** Transports T at the boundaries of the domain. T_{BC} corresponds to the first term in Eq. (11), and T_{AB} (T_{CD}) corresponds to the second (third) term.

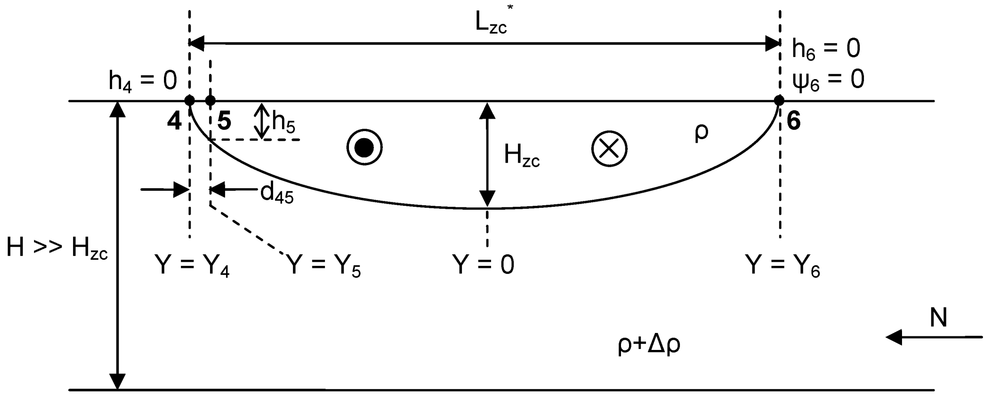

FIG. 6. Cross-sectional view of the double-frontal current (DFC) representing the train of eddies as defined by Eqs. (12a) and (12b). The meridional positions of the current's fronts are Y_4 and Y_6, its maximum depth is H_{zc} (at $Y = 0$), and its width is $L^*_{zc} = Y_4 - Y_6$. This current is asymmetrical ($|Y_4| > |Y_6|$) due to β, and it has the same transport and potential vorticity as the eddy train. The DFC has density ρ, and it is embedded in an infinitely deep layer of depth H (where $H >> H_{zc}$) and density $\rho+\Delta\rho$. Positions Y_4 and Y_5 delimit the zone of DFC net transport, which has width d_{45} and maximum depth h_5. These two variables are of $\sim O(\varepsilon^{1/2})$, and the net transport is of $O(\varepsilon)$. The net transport between points Y_5 and Y_6 is zero.

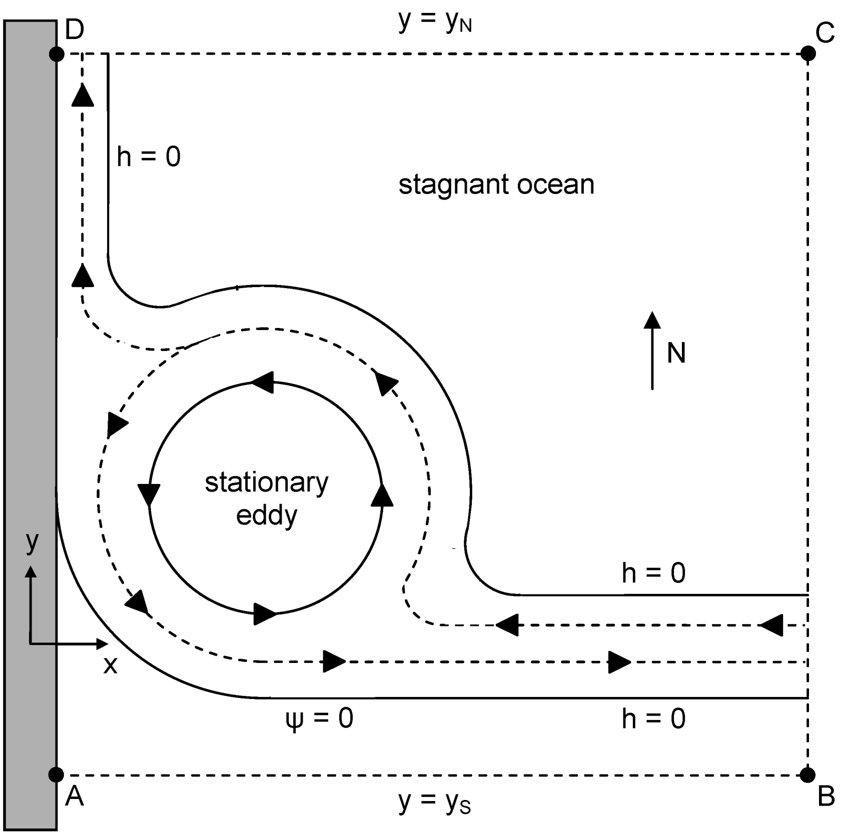

FIG. 7. Plan view of the encounter between a zonal double-frontal current and a meridional wall (gray rectangle). The current enters the domain through its eastern boundary (boundary BC). Leakage of the impinging eddies, which are here represented by the DFC, results from the wall interaction and produces a northward current (NC) that exits the domain through its northern boundary (CD). The ocean is stagnant in two regions: a large area in the north and also a smaller area in the south where the transport function ψ was assumed to be zero. In these regions, the upper layer vanishes.

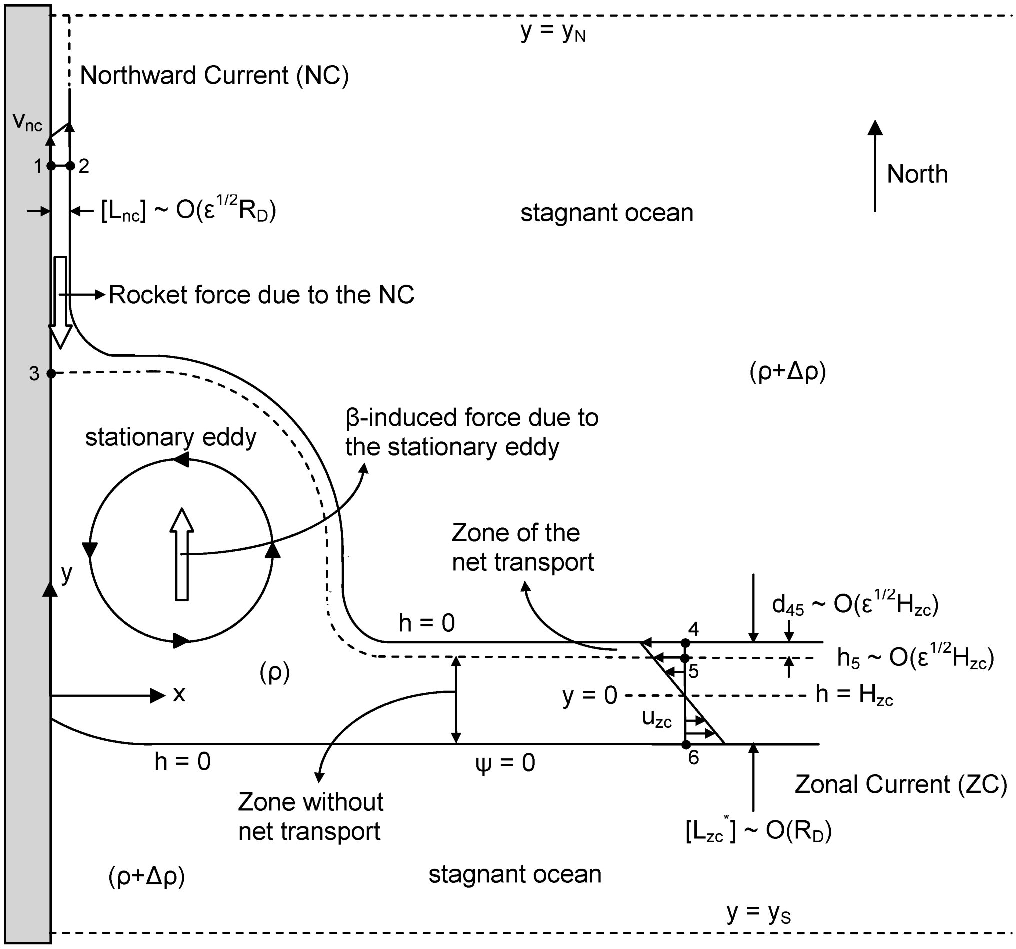

FIG. 8. Detailed plan view of the encounter between the double frontal-current and a meridional wall. The main scales [Eqs. (20) and (21)] are shown, as are the main velocity profiles [Eqs. (12a) and (23)] and the forces acting in the domain D_o. In this limiting scenario, the coordinate systems *xy* and *XY* are identical. For definition of terms, see text and previous figures.

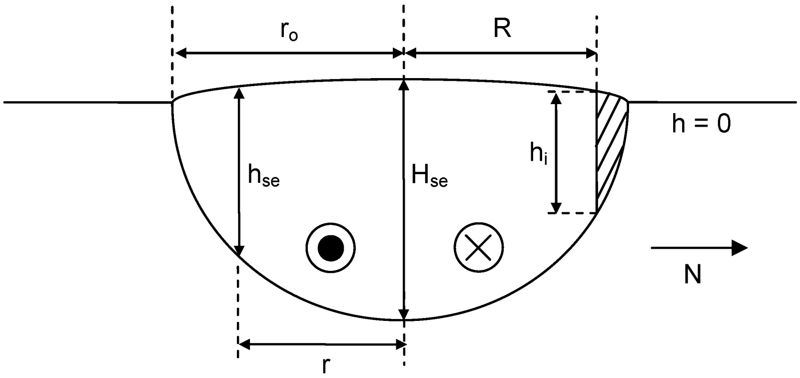

FIG. 9. Cross-sectional view of the stationary eddy (SE). The shaded zone on the northern side represents the surrounding current. The radius r_0 is the total radius of the eddy, which is measured from the eddy's center to its rim (where the eddy thickness vanishes). R is the distance from the eddy's center to the eddy–current interface; the vertical dimension of the interface is h_i. Radius r is the distance from the eddy center to any location where the eddy thickness is h_{se}. The maximum thickness of the eddy is H_{se} (at the eddy center).

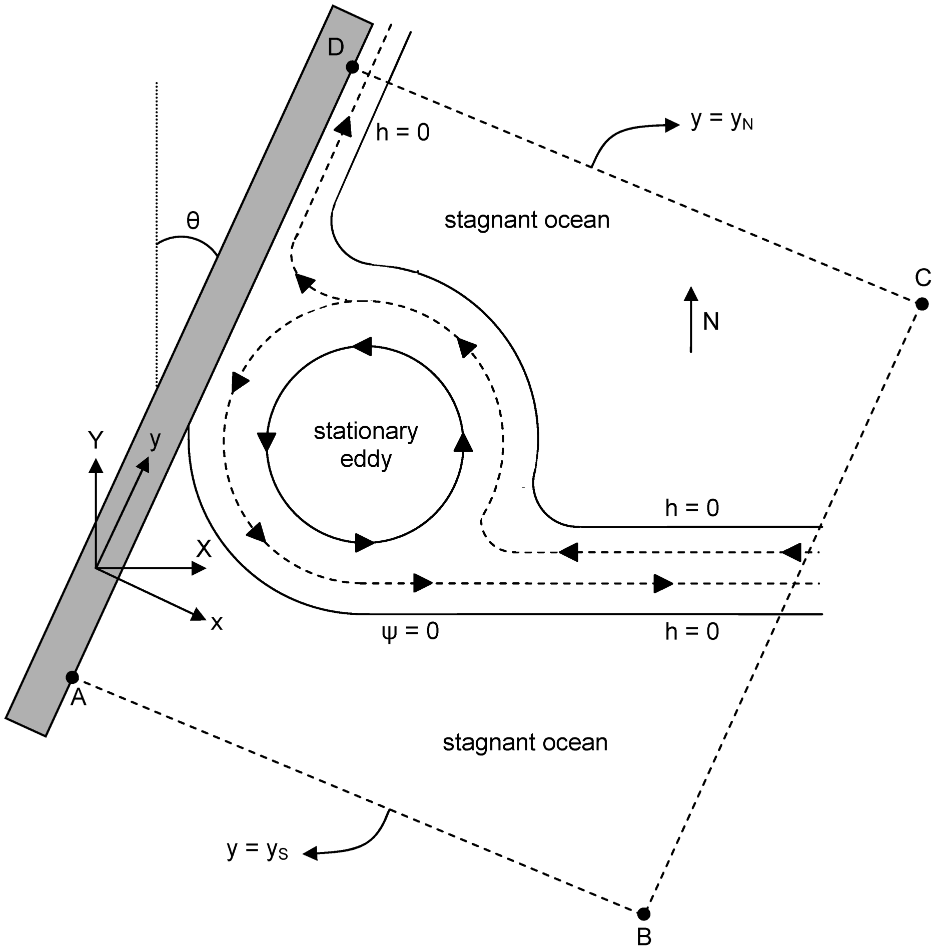

FIG. 10. Plan view of a double-frontal current with a tilted wall. The angle between the *xy* and *XY* coordinate systems is θ.

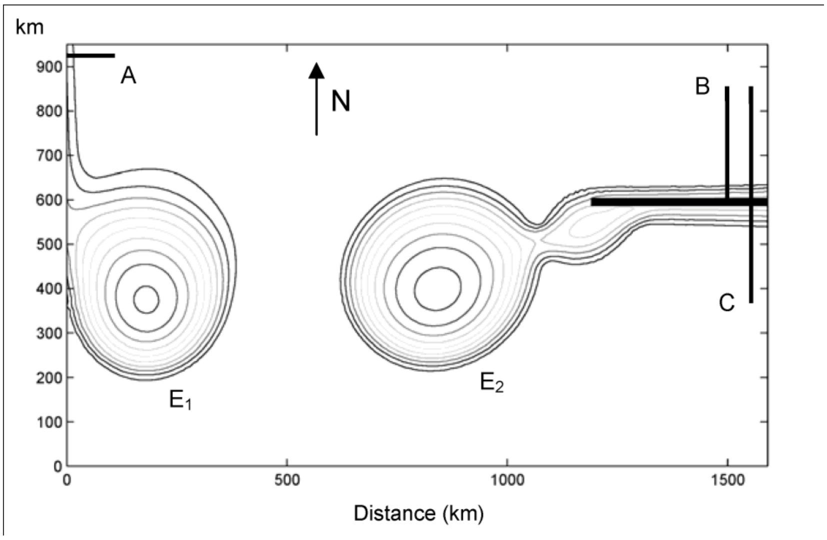

FIG. 11. Eddy thicknesses obtained in a representative eddy–wall numerical simulation (Case I, Exp. 02, Table 1). The contour interval is 300 m. This frame shows one eddy (E_1) contacting the western wall and leaking toward the north while a second eddy (E_2) is nearly pinched off from the eddy cannon on the right. Section A indicates where the transport of the leak was calculated. Eddy transport was calculated as the difference between the transports across sections B and C. Numerical stability demands an eddy viscosity of 400 m^2 s^{-1} (see text for explanation); $g' = 0.01$ m s^{-2} and $f_0 = -10^{-4}$ s^{-1}. The time step is 288 sec.

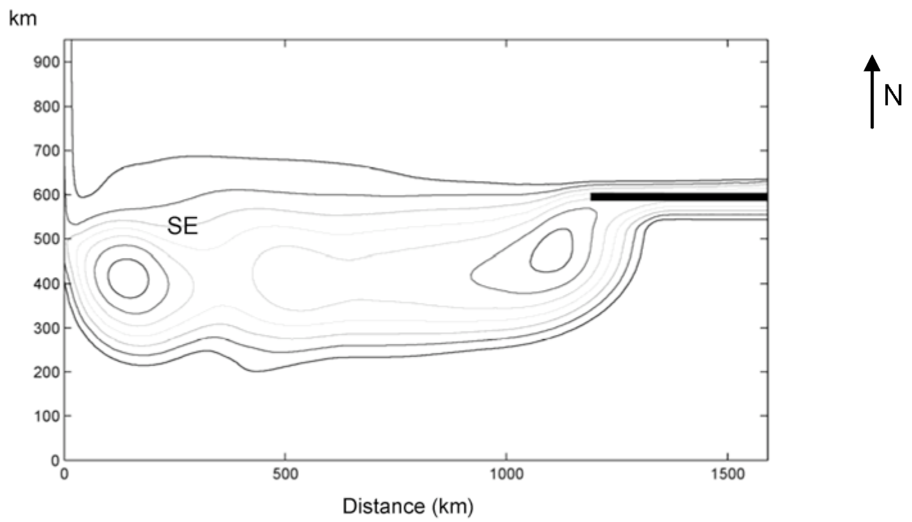

FIG. 12. Eddy train (double-frontal current) thickness for one of the numerical simulations (Case I, Exp. 02, Table 1). The DFC was generated by continuous production of eddies on the right. All other model conditions are as for Fig. 11. Note the stationary eddy (SE) generated in the DFC–wall encounter region.

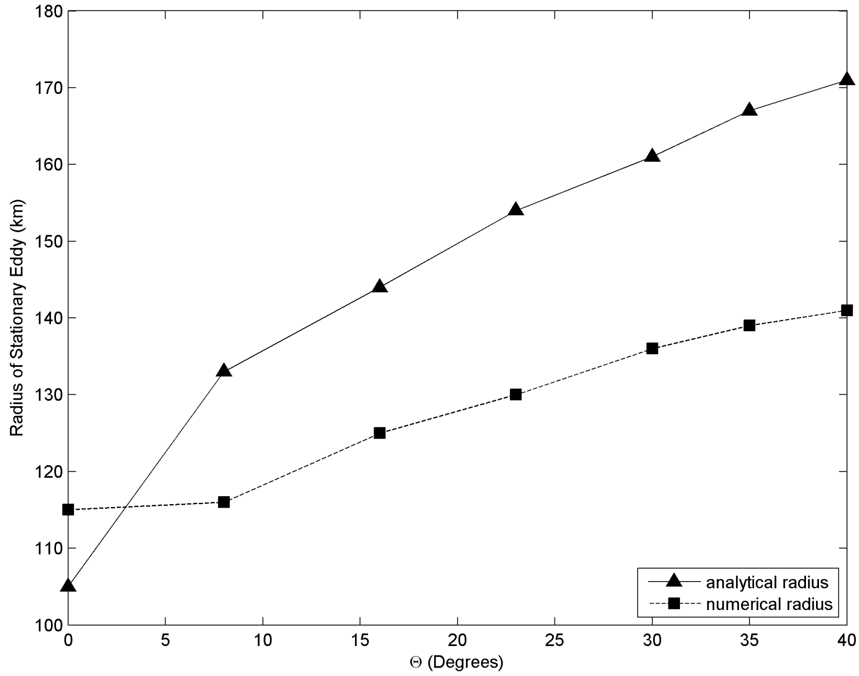

Fig. 13. Stationary eddy radii obtained for different angles of wall tilt (θ) with the analytical model and representative Case AII numerical experiments (Exp. 01–07, Table 1).